

# Freestanding and permeable nanoporous gold membranes for surface-enhanced Raman scattering

Roman M. Wyss,<sup>†, #</sup> Markus Parzefall,<sup>‡, #</sup> Cynthia M. Gruber,<sup>‡</sup> Sebastian Busschaert,<sup>‡</sup> Karl-Philipp Schlichting,<sup>§</sup> Carin Rae Lightner,<sup>||</sup> Emanuel Lörtscher,<sup>¶</sup> Lukas Novotny,<sup>‡</sup> and Sebastian Heeg<sup>\*, ‡</sup>

<sup>†</sup>*Soft Materials Department of Materials, ETH Zürich, Zürich CH-8093, Switzerland*

<sup>‡</sup>*Photonics Laboratory ETH Zürich, Zürich CH-8093, Switzerland*

<sup>¶</sup>*IBM Research - Zurich, Rüschlikon CH-8803, Switzerland*

<sup>§</sup>*Laboratory of Thermodynamics in Emerging Technologies Department of Mechanical and Process Engineering, ETH Zürich, Zürich CH-8092, Switzerland*

<sup>||</sup>*Optical Materials Engineering Laboratory, Department of Mechanical and Process Engineering, ETH Zürich, Zürich CH-8092, Switzerland*

<sup>⊥</sup>*current affiliation: Department of Physics, Humboldt Universität zu Berlin, 12489 Berlin, Germany*

<sup>#</sup>*R. M. W. and M. P. contributed equally to this work.*

E-mail: sebastian.heeg@physik.hu-berlin.de

## Abstract

Surface-enhanced Raman spectroscopy (SERS) demands reliable, high enhancement substrates in order to be used in different fields of application. Here, we introduce free-standing porous gold membranes (PAuM) as easy to produce, scalable, mechanically

stable, and effective SERS substrates. We fabricate large-scale sub-30 nm thick PAuM, that form freestanding membranes with varying morphologies depending on the nominal gold thickness. These PAuM are mechanically stable for pressures up to  $> 3$  bar, and exhibit surface-enhanced Raman scattering with local enhancement factors of  $10^4$  to  $10^5$ , which we demonstrate by wavelength-dependent and spatially resolved Raman measurements using graphene as a local Raman probe. Numerical simulations reveal that the enhancement arises from individual, nanoscale pores in the membrane acting as optical slot antennas. Our PAuM are mechanically stable, provide robust SERS enhancement for excitation power densities up to  $10^6 \text{ W cm}^{-2}$ , and may find use as a building block in flow-through sensor applications based on SERS.

## Keywords

Porous gold membrane, SERS, Nanopores

## Introduction

Surface-enhanced Raman spectroscopy is a label-free, sensitive and compound-specific analytical technique, with an increasing number of applications in biomedical, environmental and surface sciences.<sup>1,2</sup> It relies on the chemical specificity of Raman spectroscopy in combination with the electromagnetic (EM) field enhancement in the vicinity of metallic nanostructures. The enhancement arises from localized surface plasmons (LSPs) that generate strong and localized near fields close to the metal. LSPs can be tuned in frequency by the nanostructures' material, shape and size.<sup>3</sup> Particularly strong enhancement arises from 'hotspots' in the dielectric crevice between two or more metallic structures. Molecules and adsorbates located at these hotspot may experience enhancement up to a factor of  $10^9$ , enabling Raman spectroscopy down to the single molecule level.<sup>4,5</sup> Various methods for creating Au-based SERS substrates have been studied, including e-beam lithography,<sup>6</sup> self assembly<sup>7,8</sup> or templating,<sup>9</sup>

leading to a plethora of SERS structures such as densely packed gold nanoppyramids,<sup>10,11</sup> nanolits<sup>12</sup> or nanostars.<sup>13</sup> Some of the drawbacks of current Au-based SERS substrates are the demanding manufacturing processes, limited scalability, and the laser intensity damage threshold of  $\sim 10^3 - 10^4 \text{ W cm}^{-2}$ , which limits SERS sensitivity.<sup>6-11,13-18</sup>

A particular intriguing application of SERS is flow trough sensing, where an analyte is detected by its Raman signature as it passes through a nanoslit that acts as a SERS hotspot. Current designs achieve single molecule sensitivity but require several processing steps including electron beam and UV lithography, which limits scalability and cost efficiency.<sup>19</sup> An attractive alternative to nanoslits are therefore SERS hotspots formed by nanopores that naturally arise during the formation or post-processing of metallic films. Such porous thin metal films have recently received attention in various fields such as plasmonics, photovoltaics, catalysis,<sup>20</sup> and electrochemistry.<sup>21,22</sup> SERS from supported porous thin films<sup>23-26</sup> and dealloyed gold membranes have been studied, investigating their Raman enhancement as function of gap width.<sup>27,28</sup> However, to the best of our knowledge, freestanding porous SERS structures with appreciable field enhancement, the ideal central building block of a SERS-based flow-through sensor, have not been studied thus far.

Here we demonstrate the fabrication and characterization of sub-30 nm thick, freestanding porous metal membranes and establish them as efficient, permeable SERS substrates, cf. Fig.1. Our porous metal films are manufactured on wafer scale without lithographic or advanced chemical assembly techniques. In contrast to previous work, our freestanding PAuM are intrinsically porous and mechanically stable up to  $> 3$  bar of pressure, while being highly gas permeable. Using graphene placed over the membrane as a Raman probe, we observe local Raman enhancement of the order of  $10^4$  to  $10^5$  that is stable at unprecedented high excitation power densities  $\sim 10^6 \text{ W cm}^{-2}$ . Numerical simulations that take into account the nanopore geometry indicate that the enhancement arises from individual nanopores acting as hotspots for SERS. We show that the pores mimic plasmonic slot antennas—the electromagnetic complement to linear rod antennas. The porous gold membranes introduced

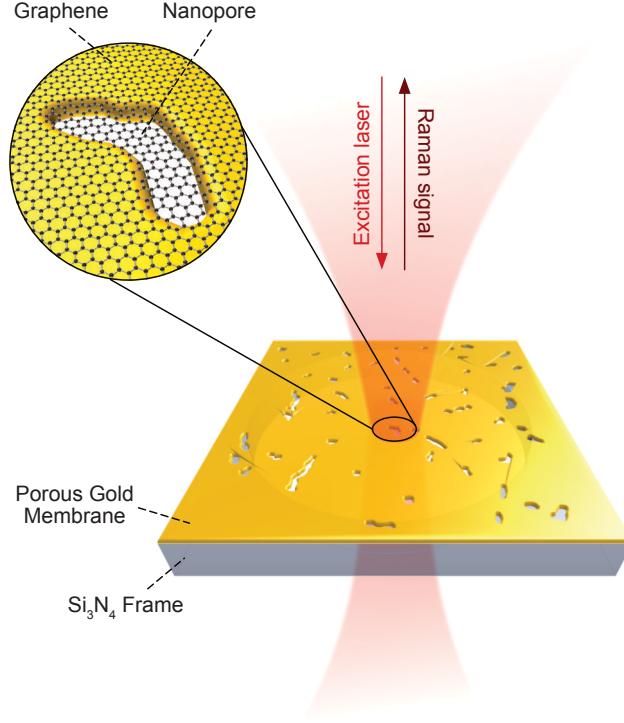


Figure 1: Illustration of a freestanding porous gold membrane that exhibits surface-enhanced Raman scattering. Graphene suspended over the nanopores probes and quantifies SERS enhancement.

in this work combine all relevant properties to act as highly effective and durable SERS substrates.

## Experiments and Results

In the following we will elaborate on the fabrication of nanoporous gold membranes and analyze the pores' basic physical properties. Next, we will study their SERS performance in terms of signal enhancement, in conjunction with numerical simulations and damage threshold.



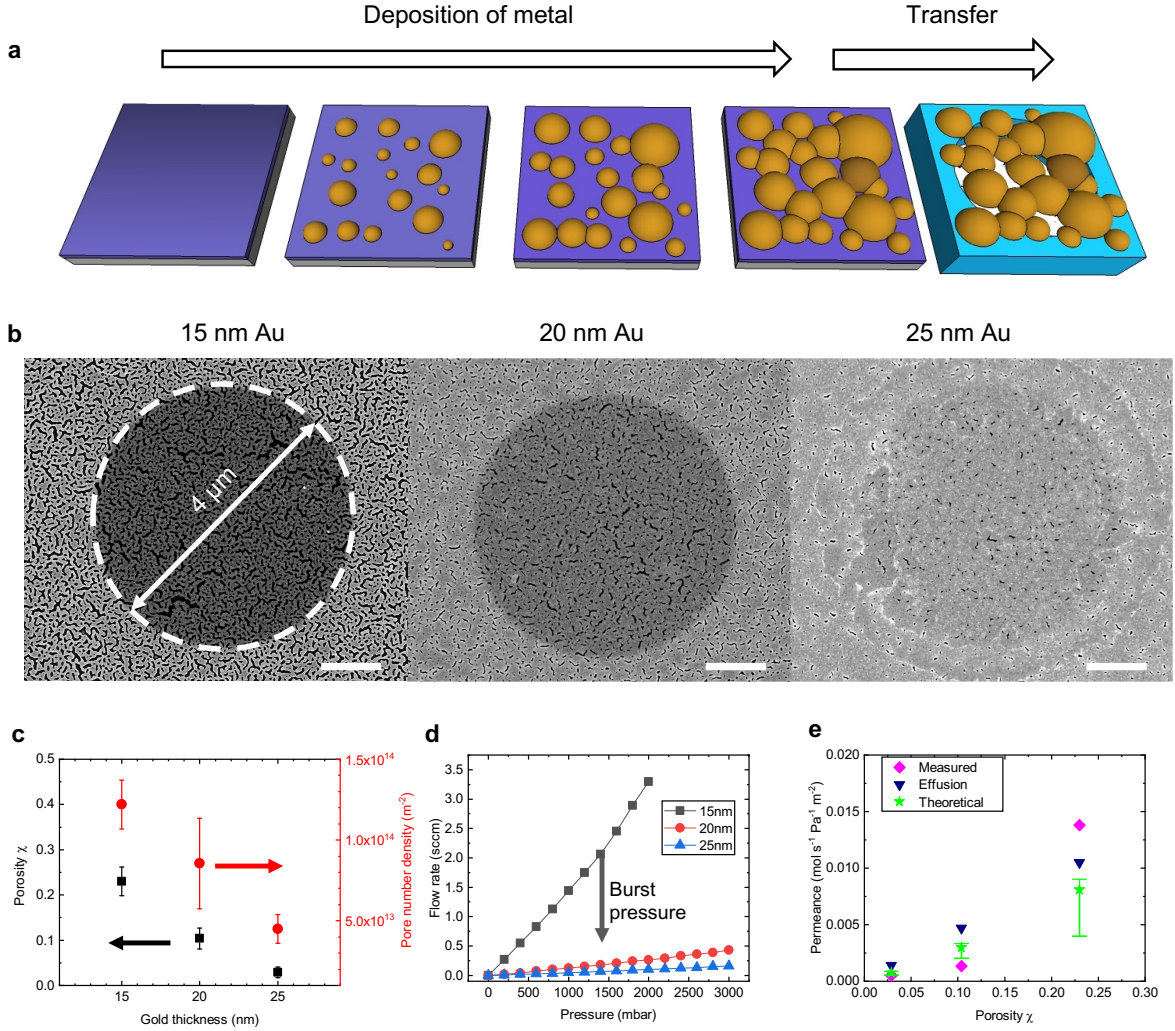


Figure 2: Porous Au membrane fabrication and characterization. (a) Schematic of the membrane manufacturing process by metal deposition via evaporation and subsequent transfer yielding freestanding porous gold membranes on  $\text{Si}_3\text{N}_4/\text{Si}$  chips. (b) Freestanding gold membranes with nominal thickness 15 nm, 20 nm and 25 nm on a single hole in the  $\text{Si}_3\text{N}_4$  chip. Scale bar: 1  $\mu\text{m}$ . (c) Porosity and pore number density as a function of nominally deposited gold thickness. (d) Gas flow versus applied pressure of Au membranes. A nonlinearity at 1500 mbar indicates material failure of the 15 nm membrane at this pressure (burst). (e) Measured and calculated permeances of porous gold membranes based on effusion and transmission probabilities.

## Membrane fabrication and characterization

Freestanding gold membranes are produced by evaporation of Gold (Au) on Silicon/Silicon dioxide (Si/SiO<sub>2</sub>) substrates and subsequent transfer to yield suspended membranes (Methods). During evaporation, the gold initially forms islands and clusters due to the different surface energies of Au ( $1.5 \text{ Jm}^{-2}$ ) and SiO<sub>2</sub> ( $0.3 \text{ Jm}^{-2}$ ) leading to nucleation and aggregation of gold clusters indicative of Volmer-Weber growth.<sup>29,30</sup> These islands grow in size and density, Fig. 2(a), up to the point where they are large enough to touch, eventually forming a percolating network. Between the islands voids persist and give rise to a porous gold film below 30 nm in thickness. While other nanoscopic gold structures have been reported to transit from ductile to brittle behavior,<sup>31,32</sup> which prevents their use as freestanding structures, our nanoporous membranes easily span over micrometer-sized holes despite their small thickness.

Scanning electron microscope (SEM) images of freestanding PAuM with thicknesses ranging from 15 nm to 25 nm are shown in Fig. 2(b) after transfer to a Si<sub>3</sub>N<sub>4</sub>/Si chip (see Methods), demonstrating that stable, freestanding membranes can be formed spanning over an  $8 \times 8$  array of  $4 \mu\text{m}$  holes. We find that 5 nm and 10 nm PAuM suffer from frequent crack formation after transfer, so they cannot be used as membranes (Supporting Information S1). Our fabrication method is readily scaled to 4 inch wafer size, with uniform pores across the entire area (Supplementary Information S1).

The pore density and porosity of the porous gold membranes are extracted from the SEM images in Fig. 2(b) and are shown in Fig. 2(c). A linearly decreasing porosity and pore number density is observed with increasing nominal Au thickness. The pores are circular and slit-like with typical radius/minor dimension of  $33.5 \pm 10.1 \text{ nm}$  for 15 nm PAuM and  $10.5 \pm 5.2 \text{ nm}$  for 25 nm PAuM, while their length can be more than 100 nm. The pore number density of  $\sim 10^{14} \text{ m}^{-2}$  is comparable to highly porous graphene membranes manufactured by self-assembly and lithographic techniques.<sup>33</sup> Though the pore size, number, and density/porosity cannot be controlled independently, highly porous membranes with controlled

pore morphology are obtained without complex manufacturing.

We characterize the gas transport through the membranes by trans-membrane pressure driven nitrogen ( $N_2$ ) flow (see Methods). The corresponding gas flow vs. pressure diagram is shown in Fig. 2(d). We extract the permeance from the linear part (0 – 1500 mbar) and plot it as a function of porosity in Fig. 2(e). As expected, the permeance increases with increasing porosity. The gas transport through thin-film membranes is governed by effusive and collective transport<sup>34</sup> as modelled in Supplementary Section S2.

The non-linearity in the flow *versus* pressure graph of the 15 nm PAuM in Fig. 2(d) indicates mechanical failure (burst) of this membrane at  $\sim 1500$  mbar. The 20 nm and 25 nm membranes, on the other hand, sustain up to 3 bar without breaking. Assuming a non-porous thin film with bulk material properties, we calculate the theoretical burst pressures  $BP_{TH}$  (bar) within film membrane theory (see Methods) and compare them to the measured burst pressures  $BP_M$  in table 1. At first sight, it might be surprising to find that  $< 30$  nm membranes sustain more than 3 bar of pressure, yet the burst pressure calculation yields values as high as 5.24 bar for a 25 nm PAuM, so that even thin film metal membranes can sustain reasonably high pressures. Taking into account, that the thin film theory predicts the burst behavior of non-porous structures, the measured and theoretical burst pressure are within reasonable agreement with each other.

Table 1: Measured burst pressures  $BP_M$  and calculated burst pressures  $BP_{TH}$  for gold membranes of 15 nm, 20 nm, and 25 nm thickness.

Membrane	$BP_M$ (bar)	$BP_{TH}$ (bar)
15 nm	1.5	3.14
20 nm	$> 3$	4.19
25 nm	$> 3$	5.24

Overall, the remarkable mechanical strength and porous metallic nature of our membranes suggest that they can be useful as easy-to-manufacture SERS substrates.

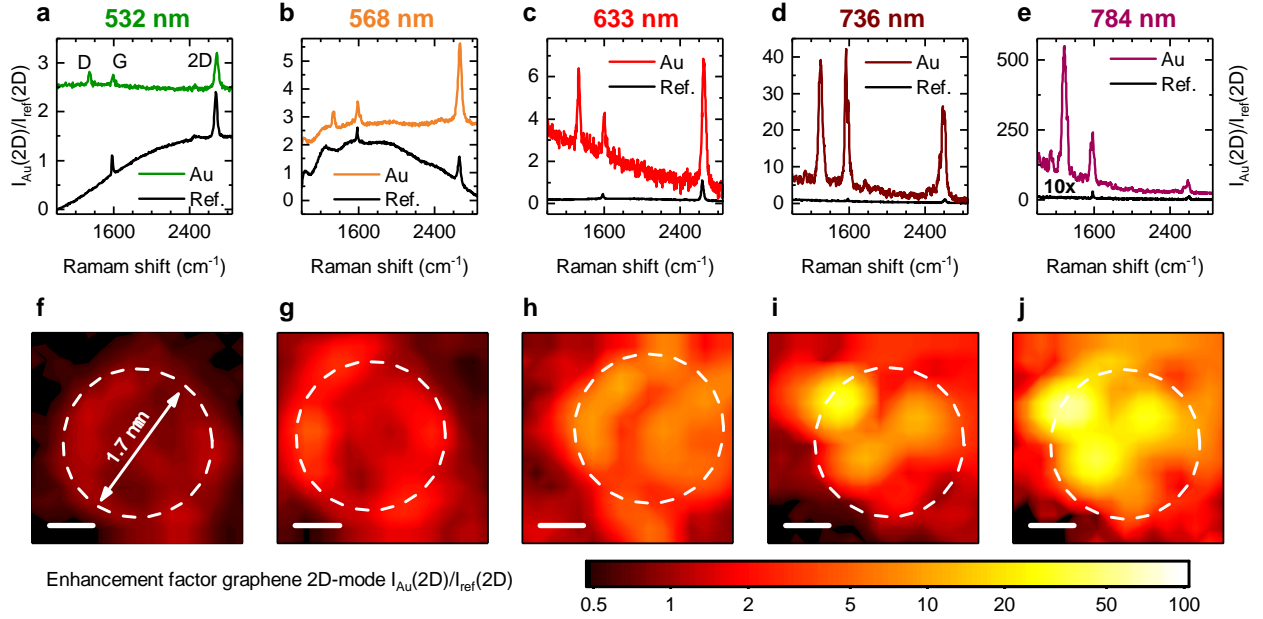


Figure 3: Wavelength-dependent SERS mapping of the nanopores in the freestanding gold membrane using graphene. Raman spectra of a graphene monolayer placed on top of a nanoporous gold membrane (thickness 25 nm) for (a) 532 nm, (b) 568 nm, (c) 633 nm, (d) 736 nm, and (e) 784 nm excitation wavelength. The intensity is normalized to the 2D mode of freestanding graphene (black) for reference. The SERS spectra in (a-e) are extracted at the locations of highest 2D intensities from Raman maps (f-j) recorded over the same circular freestanding membrane (dashed). Note that the enhancements factors displayed in (f) and (g) have been multiplied by factors of 10 and 5, respectively. Scale bar in (f-j) is 500 nm.

## Surface-enhanced Raman scattering

To develop a qualitative and quantitative understanding of SERS arising from the nanopores, we focus in the following on the 25 nm thick membrane type, c.f. Fig. 2(b). Its comparably low pore density allows us to study the enhancement arising from individual nanopores and how it is influenced by the pore geometry. Graphene is an ideal platform to probe SERS enhancement arising from plasmonic nanostructures.<sup>11,14,35–38</sup> A sheet of graphene can be easily interfaced with the nanopores by placing it on top of the PAuM, which we achieve here via a polymer-free transfer of CVD graphene, see Methods. The graphene conforms to the corrugated structure of the gold membrane and is suspended over the nanopores in the membrane as illustrated schematically in Fig. 1. Graphene then serves as a two-dimensional detection material for the local SERS enhancement—reporting the average Raman enhancement from a horizontal plane of the pore—and allowing us to correlate the pores shape and size with the SERS enhancement. Furthermore, the Raman response of graphene is independent of the excitation wavelength and polarization.<sup>39,40</sup> For graphene placed on top of the gold membranes, any dependence of its Raman signal on these parameters can hence be attributed entirely to SERS enhancement arising from the nanopores.<sup>14,17,36,38</sup>

In Figs. 3(a-e) we present the Raman spectra of graphene placed on a 25 nm-PAuM for five different excitation wavelengths  $\lambda_{\text{exc}}$  between 532 nm and 784 nm. The spectra are extracted at the location of highest intensity from the Raman maps shown in Fig. 3(f-j), which we recorded over the same freestanding membrane segment, see Methods. The dashed circles in Fig. 3(f-j) mark the outline of the freestanding PAuM segment (diameter 1.7  $\mu\text{m}$ , SEM image see Fig. 4(a)). For all wavelengths, the intensity of the Raman spectra and Raman maps is normalized to the integrated 2D mode intensity of large area suspended graphene  $I_{\text{ref}}(2\text{D})$ , which we have prepared on a separate sample, see Supporting Information. Suspended graphene as a reference for SERS is beneficial because it resembles the configuration of the graphene suspended over the nanopores and is free of interference or other effects from an underlying substrate.<sup>41</sup> For reference, the Raman spectra of freestanding graphene (black)

are included in Figs. 3(a-e). The broad background appearing in the Raman spectra of suspended graphene - in particular for 532 nm and 568 nm - arises from the partial overlap of the excitation with the  $\text{Si}_3\text{N}_4$  frame below the focal plane of the objective, an effect that is otherwise suppressed by the gold membrane.

Before we discuss SERS enhancement, it is useful to compare the pristine Raman response of graphene placed on the porous Au membrane to our suspended graphene reference. In both cases, the individual peak positions of the G- and the 2D-modes and their intensity ratio 2D/G observed in Fig. 3(a) confirm the presence of single-layer graphene.<sup>39,40</sup> The drastic change in the 2D/G intensity ratio towards higher excitation wavelengths on the other hand is due to the reduced sensitivity of our Raman spectrometer at the wavelengths of the Raman scattered light (i.e. 2D mode at 990 nm for  $\lambda_{\text{exc}} = 785$  nm). Using suspended graphene as a reference, however, factors out the instrument sensitivity. Accordingly, we define the experimental SERS enhancement factors for the G- and 2D modes as  $\text{EF}_{\text{exp}} = I_{\text{Au}}/I_{\text{ref}}$ , and list the corresponding values extracted from the Raman spectra in Fig. 3(a-e) in Table 2. The D-mode just above  $1300 \text{ cm}^{-1}$  indicates the presence of defects in the CVD graphene on PAuM, while the (mechanically exfoliated) reference is largely free of defects. We therefore exclude the D-mode when evaluating SERS enhancement arising from the nanopores.

In the following we discuss SERS enhancement from the nanopores, with a particular focus on its wavelength dependence and spatial distribution. For  $\lambda = 532 \text{ nm}$ , c.f. Fig. 3(a) and (f), we do not observe any SERS enhancement, which is expected due to the d-band absorption of gold at this wavelength.<sup>35,36,42</sup> Within the circular freestanding region,  $I_{\text{Au}}(2\text{D})/I_{\text{ref}}(2\text{D})$  ranges between 0.7 and 1. Outside the freestanding region, the Raman intensities of both the G- and the 2D-mode drop noticeably, an effect that we observe for all excitation wavelengths, c.f. Fig. 3(f-j). One factor that contributes to this behavior is the high refractive index ( $n \sim 2$ ) of the  $\text{Si}_3\text{N}_4$  substrate which, compared to the suspended part of the membrane, directs a larger fraction of the Raman signal into the substrate instead of being back-scattered and collected.<sup>43</sup>

Table 2: Experimental SERS enhancement factors EF of the G- and 2D mode at locations of highest intensity in Fig. 3(a-e) for different excitation wavelengths. The experimental enhancement factors at 784 nm translate to a local enhancement of  $10^4$ - $10^5$  at the nanopore, see simulations and Fig. 4.

$\lambda(\text{nm})$	532	568	633	736	784
EF(G)	0.9	3.0	13.3	169	202
EF(2D)	1.0	4.3	10.5	42.7	60.0

For excitations at  $\lambda_{\text{exc}} = 568 \text{ nm}$ , Fig. 3(b,g), and  $\lambda_{\text{exc}} = 633 \text{ nm}$ , Fig. 3(c,h), we observe the onset and continuous increase of SERS enhancement over the entire freestanding region. We attribute this behaviour to longer nanopores with higher aspect ratios and overall area that come into resonance with the excitation, see Simulations. The maximal enhancement reaches  $\text{EF}_{\text{exp}}(\text{G}) = 13.3$  and  $\text{EF}_{\text{exp}}(2\text{D}) = 10.5$  at  $\lambda_{\text{exc}} = 633 \text{ nm}$  and remains uniform within a factor of two. It is not surprising to observe different SERS enhancement factors for the two Raman modes of graphene at the same location, as their comparably large energy separation ( $\hbar\omega_{\text{G}} \sim 200 \text{ meV}$ ,  $\hbar\omega_{2\text{D}} \sim 330 \text{ meV}$ ) leads to variations in the spectral overlap of the Raman scattered light and a given plasmonic resonance, which in turn modifies the observed enhancement.<sup>14,35</sup>

The SERS enhancement changes drastically in spatial distribution and magnitude for excitation wavelengths above 700 nm. We observe strong enhancement from three localized regions of the Au membrane, c.f. Figs. 3(d,i) and (e,j). The peak enhancement extracted from Fig. 3(e) reaches  $\text{EF}_{\text{G}} = 202$  and  $\text{EF}_{2\text{D}} = 60$  for  $\lambda_{\text{exc}} = 784 \text{ nm}$ . This suggests that the enhancement arises from very few or even single pores that act as SERS hotspots – with local enhancements of  $10^4 - 10^5$ , see Simulations – as compared the rather homogeneous enhancement observed for  $\lambda < 700 \text{ nm}$ , where many pores contribute to the overall enhancement. Importantly, these hotspots are characteristic of the entire Au-membrane and not limited to the freestanding circular region shown Fig. 3. We observed the same behavior for two additional circular freestanding regions for which wavelength-dependent Raman mapping was performed, see Supporting Information.

## Simulations

To gain insight into the origin of the observed Raman enhancement and the emergence of hotspots localized within the freestanding Au membrane towards longer excitation wavelengths, we perform numerical electrodynamics simulations of the geometry based on high-resolution scanning-electron microscope (SEM) images, as shown in Fig. 4(a) for the membrane studied in Fig. 3. Detailed information regarding the simulations is given in the Methods section.

In brief, we extract a two-dimensional map of outlines of the nanopores within and around the suspended Au membrane from the SEM image shown in Fig. 4(a). We then extrude this map to the nominal thickness of the membrane (25 nm) and simulate the enhancement of the electric field amplitude  $|\mathbf{E}|/|\mathbf{E}_0|$ , where  $|\mathbf{E}_0|$  is the amplitude of the plane wave excitation. The local Raman enhancement factor  $\text{EF}_{\text{loc}}$  is then given as<sup>1,42</sup>

$$\text{EF}_{\text{loc}} = \left( \frac{|\mathbf{E}(\lambda_{\text{exc}})|}{|\mathbf{E}_0(\lambda_{\text{exc}})|} \right)^2 \times \left( \frac{|\mathbf{E}(\lambda_{\text{em}})|}{|\mathbf{E}_0(\lambda_{\text{em}})|} \right)^2, \quad (1)$$

where  $\lambda_{\text{em}}$  is the emission wavelength of the Raman mode.

Figure 4(b) shows the simulation results of Eqn. (1) for a cross section through the center of the membrane. The simulations were carried out for  $\lambda_{\text{exc}} = 784 \text{ nm}$  and  $\lambda_{\text{em},2\text{D}} = 990 \text{ nm}$ , corresponding to the 2D Raman mode of graphene. The polarization of the exciting plane waves corresponds to the experimental polarization (cf. Methods). The simulated enhancement map is overlaid with the outlines of the nanopores as extracted from the SEM image in Figure 4(a), suggesting that, the enhancement is dominated by a few selected nanopores, in agreement with the experimental observation of localized hotspots. The simulation further suggests that—within those nanopores—the Raman enhancement locally reaches values of  $10^4$  to  $10^5$ . To allow for a direct comparison with our experiments, we further convolute the enhancement map with a two-dimensional Gaussian function, emulating the diffraction-limited nature of the confocal measurement. The results are shown in Fig. 4(c). The spatial



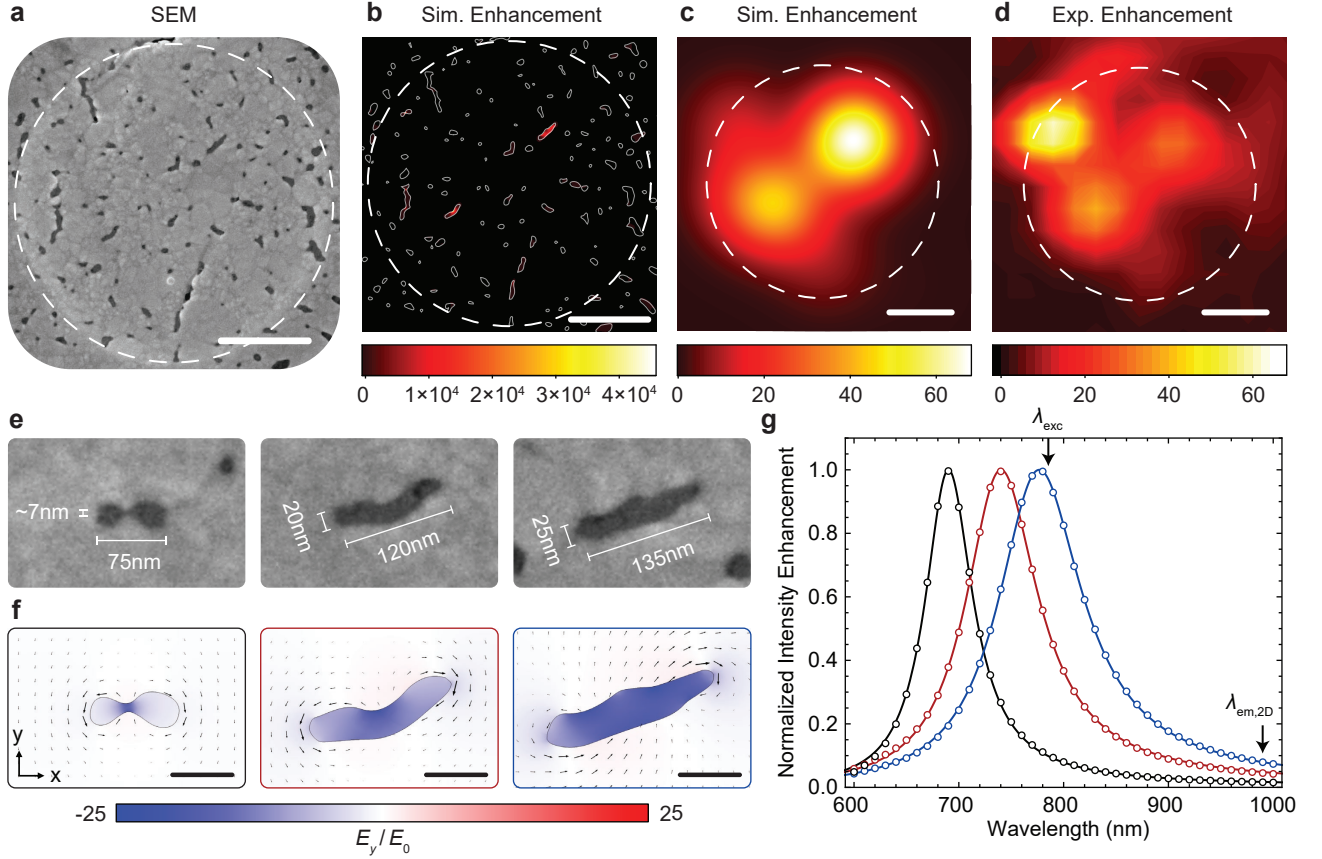


Figure 4: Numerical analysis of porous gold membranes. (a) SEM image of a freestanding Au membrane (25 nm nominal thickness), covered by monolayer graphene. (b) Simulated local enhancement  $EF_{\text{loc}}$  (cf. Eqn. (1)) of the 2D Raman mode intensity for an excitation wavelength  $\lambda_{\text{exc}}$  of 784 nm, overlaid with the outlines extracted from (a). (c) As (b), convoluted with a Gaussian function, the full width at half maximum (FWHM) of which is given by  $\lambda_{\text{exc}}/(2\text{NA})$ , where  $\text{NA} = 0.8$  is the numerical aperture of the objective. (d) Experimental map of the enhancement of the integrated 2D intensity at  $\lambda_{\text{exc}} = 784$  nm, reproducing the data shown in Fig. 3(e). (e) Magnified SEM images of three nanopores. (f) Simulated enhancement of the  $y$ -component of the electric field for the three nanopores shown in (e) under  $y$ -polarized plane wave illumination for  $\lambda_{\text{exc}} = 784$  nm. Black arrows indicate magnitude and direction of the current density. (g) Simulated, normalized intensity enhancement spectra in the center of the three nanopores (empty circles), fitted by Lorentzian functions (lines). Colors correspond to the colored frames in (f). The dashed outlines in (a-d) mark the position of the suspended membrane. Scale bar in (a-d) is 500 nm. Scale bar in (f) is 50 nm.

distribution of enhancement is in qualitatively good agreement with the corresponding experimentally obtained map displayed in Fig. 4(d). Furthermore, both experiment and simulation are in agreement regarding the absolute magnitude of the Raman enhancement. We find similarly good agreement between experiment and simulation for two additional freestanding sections of the membrane, see Supplementary Information.

Next, we carry out a detailed analysis of the three nanopores which exhibit the highest enhancement factors. Magnified SEM images of these nanopores are shown in Fig. 4(e). All three are similarly oriented and elongated along the same axis. Additionally, the first pore is narrowed down to a minimum width of  $\sim 7$  nm. Figure 4(f) further demonstrates that all three nanopores display the same electric field and current distributions, suggesting that the nanopores support localized resonances that are determined by their size and shape. These resonances are indeed observed when analyzing the intensity enhancement in the center of each nanopore as a function of wavelength, shown in Fig. 4(g). The spectral resonance positions of the two larger pores agree very well with the evolution of enhancement as a function of wavelength observed in Fig. 3(a-e). Our simulations do not reproduce the experimentally observed trend for the smallest pore. This, however, is not surprising as our simulated geometry neglects the surface morphology of the pores for reasons of computational efficiency. The morphological details have the strongest effect on resonance position and enhancement for pores that are narrower than the nominal film thickness, as is the case here. This explains the mismatch between experiment and simulation with regards to the smallest pore.

Our analysis shows that nanopores act as slot antennas—the electromagnetic complement to linear rod antennas<sup>44,45</sup>—exhibiting shape and size-dependent LSP resonances (cf. Supplementary Information). These resonances are accompanied by strongly enhanced near-fields, leading to the observed Raman intensity enhancement. Slot antennas are most efficiently excited with the electric field polarized parallel to their minor axis,<sup>46,47</sup> in agreement with the relative orientation of the three nanopores shown in Fig. 4(e,f) with respect to

the incident plane wave polarization. The resonance position of slot antennas shifts towards longer wavelengths with increased aspect ratio.<sup>48,49</sup> In addition we find that slot antennas exhibit a stronger enhancement at higher aspect ratios, as well as when they are suspended (cf. Supplementary Information). This explains both the overall increase in enhancement towards longer wavelengths as well as the localization of the highest enhancement to the suspended sections of the Au membrane, as observed in Fig. 3(a-e).

Finally, our simulations of slot antennas suggest that the enhancement is fairly constant across the entire depth of the nanopores (cf. Supplementary Information). Hence, the enhancement probed by the graphene membrane is a faithful representation of the enhancement present in the pore’s entire volume, which is the relevant figure of merit for freestanding flow-through SERS structures.

## Stable SERS under high illumination powers

The sensitivity of a SERS based sensor—the intended application of the porous gold membranes presented in this work—does not depend on the local Raman enhancement at a hotspot itself, but rather on the absolute measured SERS signal. The latter scales linearly with the excitation power. The more excitation power a SERS substrate can sustain, the better it performs as a sensor. To evaluate the stability of our 25 nm-PAuM as a SERS substrate, we recorded graphene Raman spectra at a nanopore hotspot comparable to that described in Fig. 3(e,j) and Fig. 4 at  $\lambda = 784$  nm for different excitation power densities  $P$  (see Methods). The graphene G-mode intensity  $I_{\text{Au}}^{\text{G}}(P)$  at the hotspot as a function of power density is shown in Fig. 5(a). Here  $I_{\text{Au}}^{\text{G}}(P)$  is normalized to the intensity  $I_{\text{Au}}^{\text{G}}(P)$  recorded at the lowest power density  $P_{\text{min}} \sim 4 \times 10^4 \text{ W cm}^{-2}$ , which corresponds to a power of 350  $\mu\text{W}$  in the laser focus of our setup.

Figure 5(a) shows that the enhancement of the G-mode increases linearly (solid line) with the excitation power density as  $I_{\text{Au}}^{\text{G}}(P)/I_{\text{Au}}^{\text{G}}(P_{\text{min}}) = 1.06 \pm 0.07 P/P_{\text{min}}$  between  $P_{\text{min}} \sim 4 \times 10^4 \text{ W cm}^{-2}$  and  $P \sim 1.1 \times 10^6 \text{ W cm}^{-2}$ . This behavior indicates that both the nanopore

forming the SERS hotspot and the suspended graphene membrane remain functional and deliver reliable SERS enhancement up to  $P \sim 1.1 \times 10^6 \text{ Wcm}^{-2}$ , which we confirm by cycling back to  $P_{\min}$  after every increase in  $P$  without loss in G-mode intensity, see Supporting Information. For larger power densities,  $I_{\text{Au}}^{\text{G}}(P)$  increases further without following the linear trend (dashed line). This relative decrease in SERS enhancement indicates the onset of morphological changes within the nanopore and/or damage of the graphene membrane. At  $P_{\max} \sim 4.2 \times 10^6 \text{ Wcm}^2$ , the nanopore hotspot with its graphene Raman probe eventually fails irreversibly.

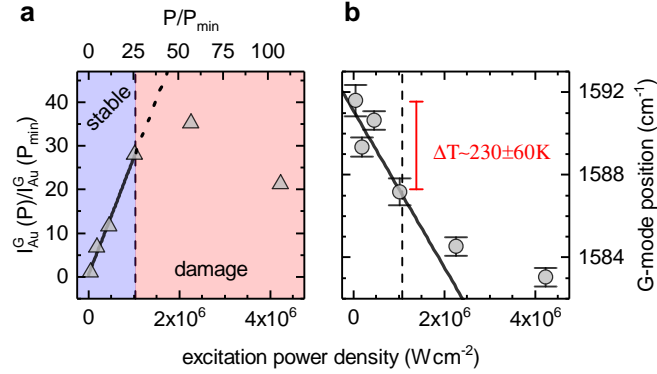


Figure 5: SERS stability under high illumination powers. (a) G-mode intensity and (b) position of graphene at a nanopore hotspot for various excitation power densities. The hotspot is stable up to  $P \sim 1.1 \times 10^6 \text{ Wcm}^{-2}$  for which the G-mode downshift suggest a local temperature increase  $\Delta T \sim 230 \text{ K}$ .

To gain insight into the failure mechanism of the SERS hotspot, we extract the local temperature from the change of the G-mode position of graphene with increasing laser power, Fig. 5(b). For  $P = 1.1 \times 10^6 \text{ Wcm}^{-2}$ , the highest power with stable SERS enhancement, the G-mode is downshifted by  $3.6 \pm 0.9 \text{ cm}^{-1}$  with respect to  $P_{\min}$ , which corresponds to a temperature increase of  $230 \pm 60 \text{ K}$  (see Methods).<sup>50</sup> Assuming no significant heating for  $P_{\min}$  and thermal equilibrium between the suspended graphene and the Au membrane, we infer a local hotspot temperature of  $\sim 525 \pm 60 \text{ K}$ , low compared to the melting point of bulk gold ( $\sim 1330 \text{ K}$ ), nanometer-scale gold nanoparticles ( $\geq 950 \text{ K}$ ),<sup>51</sup> as well as the breakdown temperature of graphene in air ( $875 \text{ K}$ ).<sup>52</sup> For  $P = 2.2 \times 10^6 \text{ Wcm}^{-2}$ , the linear

trend in Fig. 5(b) suggests that the nanopore-graphene system fails at a local temperature of around 855 K. A temperature-induced breakdown of the suspended graphene Raman probe is therefore rather unlikely. It should be noted, however, that the diffusion of gold atoms is non-negligible at room temperature. We, therefore, hypothesize that the most likely failure mechanism is the disintegration of the hotspots due to the accelerated gold diffusion and the simultaneous reshaping of the membrane.

## Discussion

Compared to alternative SERS substrates, our porous Au membranes show an outstanding durability with respect to illumination power. The membrane acts as its own heat sink thanks to the superior heat conduction inherent to metals and the corresponding efficient heat dissipation away from the illuminated area. Stable SERS enhancement for  $P = 1.1 \times 10^6 \text{ W cm}^{-2}$  exceeds the limits reported in the literature for conventional self-assembled ( $\sim 10^3 \text{ W cm}^{-2}$ ) and lithographically fabricated metallic SERS nanostructures ( $\sim 10^3 - 10^4 \text{ W cm}^{-2}$ ) by up to three orders of magnitude,<sup>6-9,14-18</sup> see Supporting information for an overview, and demonstrates the extraordinary thermal stability of nanoporous Au membranes introduced in this work.

The  $10^2 - 10^3$ -fold increase in excitation power that can be sustained by our Au-membranes as compared to alternative SERS substrates corresponds directly to a  $10^2 - 10^3$ -fold increase in total SERS signal and hence SERS sensitivity. This compensates for the weaker maximum local SERS enhancement of the nanopores ( $\sim 10^5$ ) compared to that reported for hotspots of supported Au dimers with sub-nm gaps (up to  $\sim 10^8 - 10^9$ ).<sup>15</sup> The nanopores, on the other hand, provide enhancement over far greater volumes than sub-nm hotspots, which makes them particularly suitable as permeable SERS sensor.

In this work, we chose to focus on the 25 nm thick membrane with the lowest available pore density, as this allowed us to assess the performance of PAuM based on isolated pores

that act as SERS hotspots. Large scale Raman mapping of the 20 nm thick PAuM (see Supporting information) shows that the total SERS enhancement increases approximately linearly with the pore number density, c.f. Fig 2, and becomes more spatially homogeneous. The optimal PAuM thickness for a particular SERS experiment or application will depend on the specific needs with respect to permeance, mechanical stability, hotspot density and overall SERS enhancement.

## Conclusions

In conclusion, we have introduced freestanding nanoporous gold membranes as a simple, scalable, novel and effective SERS platform. Our suspended gold films of 15 nm - 25 nm thickness are highly porous and mechanically stable up to  $> 3$  bar of pressure, allowing for their use as on-surface as well as permeable SERS substrates. Using graphene as a Raman probe in combination with excitation energy dependent Raman mapping, we observe a  $10^5$  SERS enhancement from hotspots formed by individual nanopores, in agreement with numerical simulations. A general benefit of freestanding SERS structures is an increased emission of the Raman scattered light into the detection half-space compared to supported structures. Our Au membranes withstand excitation powers up to  $10^6 \text{ W cm}^{-2}$  – adding two orders of magnitude to their sensitivity as compared to conventional SERS nanostructures – with moderate temperatures at the nanopore hotspots. Optimizing the fabrication parameters towards nanopores with a preferential size, shape and orientation, i.e. by pre patterning the substrate for membranes formation, has the potential to achieve even higher and more homogeneous enhancement.

# Methods

## Manufacturing and Transfer of porous Ai membranes

Au membranes are produced by e-beam evaporation of Au (Evatec, deposition rate 0.2 nm/s, distance from source: 600 mm) on Silicon (Si) wafers with 30 nm thick thermally grown silicon dioxide ( $\text{SiO}_2$ ). The wafers have been cleaned by acetone-isopropyl alcohol rinsing followed by 1 min of oxygen plasma (600W,  $\text{O}_2$  flow 25 sccm, TePla). The nominal thickness of the PAuM membranes manufactured here are 5 nm, 10 nm, 15 nm, 20 nm and 25 nm as indicated by the quartz crystal.

The porous gold films are transferred similarly to 2D materials, such as graphene, to yield freestanding membranes.<sup>53,54</sup> A 120 nm thick polymethylmethacrylate (PMMA, in Anisol 2 w%) protection layer is coated and subsequently floating etched in buffered hydrofluoric acid (BHF). Under-etching leads to release of the Au/PMMA from the Si wafer resulting in a floating film, which is rinsed  $2 \times 20$  min in DI-water and transferred to a Si/ $\text{Si}_3\text{N}_4$  substrate with arrays of holes forming freestanding PAuM.

Chips with holes of  $4 \mu\text{m}$  in arrays of  $8 \times 8$  are manufactured following the procedure from ref.<sup>34</sup> In brief, wafers (from Si-Mat, 150nm  $\text{Si}_3\text{N}_4$  on Si, ultra low stress) are photolithographically defined and etched by fluor-based chemistry using reactive ion etching (RIE) and subsequent KOH etching to form freestanding  $\text{Si}_3\text{N}_4$  membranes. Into these freestanding  $\text{Si}_3\text{N}_4$  membranes, the holes are defined lithographically and etched by RIE.

## Burst pressure calculation based on thin film theory

For a thin membrane on a circular support of diameter  $D$  we can assume that the membrane is only loaded by in-plane stress, where the burst pressure is defined by

$$\Delta P = \frac{t}{D} \sqrt{\frac{96(1.026 - 0.79\nu - 0.233\nu^2)\sigma^3}{E}}, \quad (2)$$

where  $E = 79$  GPa is the Young's modulus,  $\nu = 0.4$  is the Poisson ratio,  $\sigma = 220$  MPa is the breaking strength,  $t$  is the membrane thickness and  $D = 4 \times 10^{-6}$  m is the diameter of the support hole. In this calculation, the porosity of the gold membrane is neglected leading to an upper bound value for the burst pressure.

## Support-free transfer of graphene to porous gold

Graphene was grown in a cold-wall chemical vapor deposition (Aixtron ltd.) as described in Ref.<sup>34</sup> yielding predominately monolayer graphene on copper (Alfa Aesar 46986). To avoid contamination of graphene by polymer residues, graphene was transferred polymer-free, following the method reported in Ref.<sup>55</sup> The as-grown graphene on copper is placed at the interface of copper etchant (0.5M ammonium persulfate (APS)) and hexane. Once the copper has dissolved entirely, the graphene is removed from the etchant and placed at the interface of DI-water hexane, and rinsed for 30 min before being scooped with the target substrate and dried.

## Raman spectroscopy

Wavelength dependent Raman mapping was performed on a home-built Raman setup equipped with a xy-Piezo stage (MadCity Labs) in backscattering configuration using a  $100\times$  (NA 0.9) objective. A Coherent Innova 70C Ar/Kr laser (532 nm, 568 nm), a Thorlabs HeNe laser (633 nm) and a wavelength tunable Ti:Sa laser (736 nm, 784 nm) served as linearly polarized excitation sources. For all excitation wavelengths, the laser power was kept below 1.5 mW for graphene on the PAuM and below 0.5 mW for the suspended graphene reference. For each wavelength, the reference was measured directly after taking a Raman map without changing any instrument parameters. Integration times were up to 10 s for the maps and up to 90 s for the reference. The Raman maps were acquired with 150 nm step-size. The polarization in all Raman measurements was set to  $22.5^\circ$  from the vertical axis in Fig. 3.

Power dependent measurements were performed on a Horiba LabRam HR Evolution



system equipped with a 785 nm Toptica XTRA II high power single frequency diode laser and a LMPLFLN100X Olympus objective (NA 0.9). The laser power was measured after the objective mount but without the objective. Taking into account the transmission efficiency of our objective (75% at 785 nm) and the overfilling of the objective's back aperture, the effective power in the laser focus given in the main paper amounts to 50 % of the measured power.

The local temperature  $T$  can be extracted from the graphene G-mode position  $\omega$  using the relation  $T = (\omega - \omega_0)\chi^{-1}$ , where  $\omega_0$  is the room-temperature peak position and  $\chi = -1.62 \times 10^{-2} \text{ cm}^{-1}\text{K}^{-1}$  is the temperature coefficient describing the G-mode's shift in position per 1 K change in temperature.<sup>50</sup>

## Scanning electron microscopy and image analysis

SEM was performed using a dual beam (FEI Helios) and a single beam (FEI Magellan) system at 5 kV acceleration voltage and 50 pA current. The pore dimensions were extracted from the SEM images using the software ImageJ.

## Gas flow measurements

The permeance was characterized using a self-built setup described in detail elsewhere.<sup>34</sup> In short, the membrane is placed in a fixture with the gold facing upstream. A mass flow controller (MFC MKS) is used to increase the pressure on the feed side of the membrane, observed by a manometer. Downstream, a mass flow meter (MFM MKS) is used to record the flow rate, which is converted to molar permeance by normalizing with the applied pressure and the total freestanding area of the membrane ( $\sim 800 \mu\text{m}^2$ ).

## Simulations

Numerical finite element simulations were carried out using the wave optics module within the commercial software package COMSOL Multiphysics 5.3a. Outlines of the nanopores across a  $1.8 \times 1.8 \mu\text{m}^2$  large region of the Au membranes are extracted from high resolution SEM images, including the circular suspended region which is  $1.7 \mu\text{m}$  in diameter. These outlines are further extruded to the nominal height of 25 nm of the membrane. Both half-spaces below and above as well as the pores within the membrane are filled with vacuum ( $n = 1$ ). Empirical values are used for the dielectric function of gold.<sup>56</sup> The field enhancement  $|\mathbf{E}(\lambda)| / |\mathbf{E}_0(\lambda)|$  at a given wavelength  $\lambda$  is determined in two steps. First, we simulate the fields for a planar gold film without nanopores under plane wave illumination. Second, we determine the altered fields in the presence of nanopores.

## Data Availability

The data that support the findings of this study are available from the corresponding author upon reasonable request.

## Supporting Information Available

S1 - Characterization of freestanding Au membranes with 5-25 nm thickness; S2 - Gas transport through Au Membranes; S3 - Freestanding graphene as Raman reference; S4 - SERS of two additional graphene covered, suspended Au-membranes. S5 - Numerical analysis of regular slot antennas in a thin Au film. S6 - SERS stability under high illumination powers. S7 - Large-scale SERS mapping of 20 nm thick porous Au membrane.

## Acknowledgements

R.M.W. acknowledges the Binnig and Rohner Nanotechnology Center. S.H. acknowledges financial support by ETH Zürich Career Seed Grant SEED-16 17-1 and by the German Research Foundation's (DFG) Emmy Noether Programme (project number 433878606). This research was partially funded by Swiss National Science Foundation (grant no. 200020\_192362/1). The authors thank N.Clark for providing the suspended graphene reference sample and acknowledge the use of the facilities at the Scientific Center for Optical and Electron Microscopy (ScopeM) at ETH Zürich.

## Author contributions

S.H. and R.M.W. conceived the project. R.M.W. manufactured and characterized the gold membranes. K.P.S. synthesized and transferred graphene. S.H. performed and evaluated the Raman measurements. S.B. performed SEM imaging. C.G., C.L. and E.L. contributed to the initial Raman characterization. M.P. performed all numerical simulations. R.M.W., M.P. and S.H. jointly interpreted the data, discussed the results and wrote the manuscript. All authors participated in the interpretation of the data and contributed to the final manuscript. R.M.W. and M.P. contributed equally to this work. S.H. coordinated and supervised the project.

## Competing financial interests

R.M.W. holds a patent for the manufacturing process of porous gold membranes ( EP18207023.5). The authors declare no other financial interests.

## References

- (1) McNay, G.; Eustace, D.; Smith, W. E.; Faulds, K.; Graham, D. Surface-enhanced Raman scattering (SERS) and surface-enhanced resonance Raman scattering (SERRS): a review of applications. *Applied spectroscopy* **2011**, *65*, 825–837.
- (2) Langer, J. et al. Present and Future of Surface-Enhanced Raman Scattering. *ACS Nano* **2019**,
- (3) Anker, J. N.; Hall, W. P.; Lyandres, O.; Shah, N. C.; Zhao, J.; Van Duyne, R. P. *Nanoscience And Technology: A Collection of Reviews from Nature Journals*; World Scientific, 2010; pp 308–319.
- (4) Nie, S.; Emory, S. R. Probing single molecules and single nanoparticles by surface-enhanced Raman scattering. *science* **1997**, *275*, 1102–1106.
- (5) Kneipp, K.; Wang, Y.; Kneipp, H.; Perelman, L. T.; Itzkan, I.; Dasari, R. R.; Feld, M. S. Single molecule detection using surface-enhanced Raman scattering (SERS). *Physical review letters* **1997**, *78*, 1667.
- (6) Abu Hatab, N. A.; Oran, J. M.; Sepaniak, M. J. Surface-enhanced Raman spectroscopy substrates created via electron beam lithography and nanotransfer printing. *ACS Nano* **2008**, *2*, 377–385.
- (7) Scarabelli, L.; Coronado-Puchau, M.; Giner-Casares, J. J.; Langer, J.; Liz-Marzan, L. M. Monodisperse gold nanotriangles: size control, large-scale self-assembly, and performance in surface-enhanced Raman scattering. *ACS Nano* **2014**, *8*, 5833–5842.
- (8) Fang, J.; Du, S.; Lebedkin, S.; Li, Z.; Kruk, R.; Kappes, M.; Hahn, H. Gold mesostructures with tailored surface topography and their self-assembly arrays for surface-enhanced Raman spectroscopy. *Nano letters* **2010**, *10*, 5006–5013.

- (9) Kondo, T.; Matsumoto, F.; Nishio, K.; Masuda, H. Surface-enhanced Raman scattering on ordered gold nanodot arrays prepared from anodic porous alumina mask. *Chemistry letters* **2008**, *37*, 466–467.
- (10) Wang, P.; Liang, O.; Zhang, W.; Schroeder, T.; Xie, Y. Ultra-Sensitive Graphene-Plasmonic Hybrid Platform for Label-Free Detection. *Advanced Materials* **2013**, *25*, 4918–4924.
- (11) Wang, P.; Zhang, W.; Liang, O.; Pantoja, M.; Katzer, J.; Schroeder, T.; Xie, Y.-H. Giant optical response from graphene-plasmonic system. *ACS Nano* **2012**, *6*, 6244–6249.
- (12) Chen, C.; Hutchison, J. A.; Dorpe, P. V.; Kox, R.; Vlaminck, I. D.; Uji-i, H.; Hofkens, J.; Lagae, L.; Maes, G.; Borghs, G. Focusing Plasmons in Nanoslits for Surface-Enhanced Raman Scattering. *Small* **2009**, *5*, 2876–2882.
- (13) Hao, F.; Nehl, C. L.; Hafner, J. H.; Nordlander, P. Plasmon resonances of a gold nanostar. *Nano letters* **2007**, *7*, 729–732.
- (14) Wasserroth, S.; Bisswanger, T.; Mueller, N. S.; Kusch, P.; Heeg, S.; Clark, N.; Schedin, F.; Gorbachev, R.; Reich, S. Graphene as a local probe to investigate near-field properties of plasmonic nanostructures. *Physical Review B* **2018**, *97*, 155417.
- (15) Zhu, W.; Crozier, K. B. Quantum mechanical limit to plasmonic enhancement as observed by surface-enhanced Raman scattering. *Nature communications* **2014**, *5*, 5228.
- (16) Mueller, N. S.; Heeg, S.; Alvarez, M. P.; Kusch, P.; Wasserroth, S.; Clark, N.; Schedin, F.; Parthenios, J.; Papagelis, K.; Galiotis, C., et al. Evaluating arbitrary strain configurations and doping in graphene with Raman spectroscopy. *2D Materials* **2017**, *5*, 015016.

- (17) Heeg, S.; Oikonomou, A.; Fernandez-Garcia, R.; Lehmann, C.; Maier, S. A.; Vijayaraghavan, A.; Reich, S. Plasmon-enhanced Raman scattering by carbon nanotubes optically coupled with near-field cavities. *Nano letters* **2014**, *14*, 1762–1768.
- (18) Heeg, S.; Clark, N.; Vijayaraghavan, A. Probing hotspots of plasmon-enhanced Raman scattering by nanomanipulation of carbon nanotubes. *Nanotechnology* **2018**, *29*, 465710.
- (19) Chen, C.; Li, Y.; Kerman, S.; Neutens, P.; Willems, K.; Cornelissen, S.; Lagae, L.; Stakenborg, T.; Dorpe, P. V. High spatial resolution nanoslit SERS for single-molecule nucleobase sensing. *Nature Communications* **2018**, *9*.
- (20) Zhang, R.; Olin, H. Porous gold films—a short review on recent progress. *Materials* **2014**, *7*, 3834–3854.
- (21) Ding, Y.; Kim, Y.; Erlebacher, J. Nanoporous gold leaf: “Ancient technology”/advanced material. *Advanced Materials* **2004**, *16*, 1897–1900.
- (22) Yu, F.; Ahl, S.; Caminade, A.-M.; Majoral, J.-P.; Knoll, W.; Erlebacher, J. Simultaneous excitation of propagating and localized surface plasmon resonance in nanoporous gold membranes. *Analytical chemistry* **2006**, *78*, 7346–7350.
- (23) Yan, A.; Hua, Y.; Dravid, V. P. Locally enhanced surface plasmons and modulated “hot-spots” in nanoporous gold patterns on atomically thin MoS<sub>2</sub> with a comparison to SiO<sub>2</sub> substrate. *Applied Physics Letters* **2016**, *108*, 091901.
- (24) Novikov, S. M.; Beermann, J.; Frydendahl, C.; Stenger, N.; Coello, V.; Mortensen, N. A.; Bozhevolnyi, S. I. Enhancement of two-photon photoluminescence and SERS for low-coverage gold films. *Optics express* **2016**, *24*, 16743–16751.
- (25) Qian, L. H.; Yan, X. Q.; Fujita, T.; Inoue, A.; Chen, M. W. Surface enhanced Ra-

- man scattering of nanoporous gold: Smaller pore sizes stronger enhancements. *Applied Physics Letters* **2007**, *90*, 153120.
- (26) Jiao, Y.; Ryckman, J. D.; Ciesielski, P. N.; Escobar, C. A.; Jennings, G. K.; Weiss, S. M. Patterned nanoporous gold as an effective SERS template. *Nanotechnology* **2011**, *22*, 295302.
- (27) Qian, L.; Yan, X.; Fujita, T.; Inoue, A.; Chen, M. Surface enhanced Raman scattering of nanoporous gold: Smaller pore sizes stronger enhancements. *Applied Physics Letters* **2007**, *90*, 153120.
- (28) Lang, X.; Qian, L.; Guan, P.; Zi, J.; Chen, M. Localized surface plasmon resonance of nanoporous gold. *Applied Physics Letters* **2011**, *98*, 093701.
- (29) Petrov, I.; Barna, P.; Hultman, L.; Greene, J. Microstructural evolution during film growth. *Journal of Vacuum Science & Technology A: Vacuum, Surfaces, and Films* **2003**, *21*, S117–S128.
- (30) Schwartzkopf, M.; Buffet, A.; Körstgens, V.; Metwalli, E.; Schlage, K.; Benecke, G.; Perlich, J.; Rawolle, M.; Rothkirch, A.; Heidmann, B., et al. From atoms to layers: in situ gold cluster growth kinetics during sputter deposition. *Nanoscale* **2013**, *5*, 5053–5062.
- (31) Li, R.; Sieradzki, K. Ductile-brittle transition in random porous Au. *Physical Review Letters* **1992**, *68*, 1168.
- (32) Biener, J.; Hodge, A. M.; Hamza, A. V. Microscopic failure behavior of nanoporous gold. *Applied Physics Letters* **2005**, *87*, 121908.
- (33) Choi, K.; Droudian, A.; Wyss, R. M.; Schlichting, K.-P.; Park, H. G. Multifunctional wafer-scale graphene membranes for fast ultrafiltration and high permeation gas separation. *Science advances* **2018**, *4*, eaau0476.

- (34) Celebi, K.; Buchheim, J.; Wyss, R. M.; Droudian, A.; Gasser, P.; Shorubalko, I.; Kye, J.-I.; Lee, C.; Park, H. G. Ultimate Permeation Across Atomically Thin Porous Graphene. *Science* **2014**, *344*, 289–292.
- (35) Heeg, S.; Fernandez-Garcia, R.; Oikonomou, A.; Schedin, F.; Narula, R.; Maier, S. A.; Vijayaraghavan, A.; Reich, S. Polarized plasmonic enhancement by Au nanostructures probed through Raman scattering of suspended graphene. *Nano letters* **2012**, *13*, 301–308.
- (36) Schedin, F.; Lidorikis, E.; Lombardo, A.; Kravets, V. G.; Geim, A. K.; Grigorenko, A. N.; Novoselov, K. S.; Ferrari, A. C. Surface-enhanced Raman spectroscopy of graphene. *ACS Nano* **2010**, *4*, 5617–5626.
- (37) Kravets, V.; Schedin, F.; Jalil, R.; Britnell, L.; Novoselov, K.; Grigorenko, A. Surface hydrogenation and optics of a graphene sheet transferred onto a plasmonic nanoarray. *The Journal of Physical Chemistry C* **2012**, *116*, 3882–3887.
- (38) Heeg, S.; Oikonomou, A.; Garcia, R. F.; Maier, S. A.; Vijayaraghavan, A.; Reich, S. Strained graphene as a local probe for plasmon-enhanced Raman scattering by gold nanostructures. *physica status solidi (RRL)–Rapid Research Letters* **2013**, *7*, 1067–1070.
- (39) Graf, D.; Molitor, F.; Ensslin, K.; Stampfer, C.; Jungen, A.; Hierold, C.; Wirtz, L. Spatially resolved Raman spectroscopy of single-and few-layer graphene. *Nano letters* **2007**, *7*, 238–242.
- (40) Ferrari, A. C.; Basko, D. M. Raman spectroscopy as a versatile tool for studying the properties of graphene. *Nature nanotechnology* **2013**, *8*, 235.
- (41) Yoon, D.; Moon, H.; Son, Y.-W.; Choi, J. S.; Park, B. H.; Cha, Y. H.; Kim, Y. D.; Cheong, H. Interference effect on Raman spectrum of graphene on SiO<sub>2</sub>/Si. *Physical Review B* **2009**, *80*, 125422.



- (42) Maier, S. A. *Plasmonics: fundamentals and applications*; Springer Science & Business Media, 2007.
- (43) Novotny, L.; Hecht, B. *Principles of Nano-Optics*, 2nd ed.; Cambridge University Press: Cambridge, 2012.
- (44) Hentschel, M.; Weiss, T.; Bagheri, S.; Giessen, H. Babinet to the half: coupling of solid and inverse plasmonic structures. *Nano letters* **2013**, *13*, 4428–4433.
- (45) Yang, H. U.; Olmon, R. L.; Deryckx, K. S.; Xu, X. G.; Bechtel, H. A.; Xu, Y.; Lail, B. A.; Raschke, M. B. Accessing the optical magnetic near-field through Babinet’s principle. *ACS Photonics* **2014**, *1*, 894–899.
- (46) Gordon, R.; Brolo, A.; McKinnon, A.; Rajora, A.; Leathem, B.; Kavanagh, K. Strong polarization in the optical transmission through elliptical nanohole arrays. *Physical review letters* **2004**, *92*, 037401.
- (47) Garcia-Vidal, F. J.; Martin-Moreno, L.; Ebbesen, T.; Kuipers, L. Light passing through subwavelength apertures. *Reviews of Modern Physics* **2010**, *82*, 729.
- (48) Koerkamp, K. K.; Enoch, S.; Segerink, F. B.; Van Hulst, N.; Kuipers, L. Strong influence of hole shape on extraordinary transmission through periodic arrays of subwavelength holes. *Physical review letters* **2004**, *92*, 183901.
- (49) Garcia-Vidal, F.; Moreno, E.; Porto, J.; Martin-Moreno, L. Transmission of light through a single rectangular hole. *Physical review letters* **2005**, *95*, 103901.
- (50) Calizo, I.; Balandin, A.; Bao, W.; Miao, F.; Lau, C. Temperature dependence of the Raman spectra of graphene and graphene multilayers. *Nano letters* **2007**, *7*, 2645–2649.
- (51) Koga, K.; Ikeshoji, T.; Sugawara, K.-i. Size-and temperature-dependent structural transitions in gold nanoparticles. *Physical review letters* **2004**, *92*, 115507.

- (52) Dorgan, V. E.; Behnam, A.; Conley, H. J.; Bolotin, K. I.; Pop, E. High-Field Electrical and Thermal Transport in Suspended Graphene. *Nano Letters* **2013**, *13*, 4581–4586.
- (53) Li, X.; Cai, W.; An, J.; Kim, S.; Nah, J.; Yang, D.; Piner, R.; Velamakanni, A.; Jung, I.; Tutuc, E., et al. Large-area synthesis of high-quality and uniform graphene films on copper foils. *science* **2009**, *324*, 1312–1314.
- (54) Reina, A.; Son, H.; Jiao, L.; Fan, B.; Dresselhaus, M. S.; Liu, Z.; Kong, J. Transferring and identification of single-and few-layer graphene on arbitrary substrates. *The Journal of Physical Chemistry C* **2008**, *112*, 17741–17744.
- (55) Zhang, G.; Güell, A. G.; Kirkman, P. M.; Lazenby, R. A.; Miller, T. S.; Unwin, P. R. Versatile polymer-free graphene transfer method and applications. *ACS applied materials & interfaces* **2016**, *8*, 8008–8016.
- (56) Johnson, P. B.; Christy, R.-W. Optical constants of the noble metals. *Physical review B* **1972**, *6*, 4370.
- (57) Dushman, S. *Production and measurement of high vacuum*; General electric review, 1922.
- (58) Clausing, P. Über die Strömung sehr verdünnter Gase durch Röhren von beliebiger Länge. *Annalen der Physik* **1932**, *404*, 961–989.
- (59) Steckelmacher, W. The effect of cross-sectional shape on the molecular flow in long tubes. *Vacuum* **1978**, *28*, 269–275.
- (60) Blake, P.; Hill, E.; Castro Neto, A.; Novoselov, K.; Jiang, D.; Yang, R.; Booth, T.; Geim, A. Making graphene visible. *Applied Physics Letters* **2007**, *91*, 063124.
- (61) Botari, T.; Paupitz, R.; da Silva Autreto, P. A.; Galvao, D. S. Graphene healing mechanisms: A theoretical investigation. *Carbon* **2016**, *99*, 302–309.

## Supporting Information

### Characterization of freestanding Au membranes with 5 nm - 25 nm thickness

The pores in the Au membranes of 15 nm to 25 nm in thickness are slit-like and circular (Fig. 6). While they can be longer than 100 nm, their minor dimension and radius are within a relatively narrow band. Using ImageJ, we extracted the area of  $\sim 100 - 150$  pores for characterization using an equivalent diameter modelling them as round pores.

Uniform and large-scale porous gold membranes on polycarbonate-track-etched (PCTE) can be formed, demonstrating the ability to yield thin-film porous metal membranes on a polymer support as large as a 4-inch wafer, shown for a 20 nm-thick PAuM in Fig. 7(a), with a homogeneous pore diameter and pore number density shown in Figs. 7(b) and (c), respectively.

### Gas transport through Au Membranes

To describe gas flow through our membranes is based on transmission probabilities, and that purely viscous or effusive transport are insufficient to describe our experimental observations. In general,  $N_2$  flow through thin membranes with pores in the range  $< 50$  nm cannot be described by viscous transport as the mean free path (MFP) at standard temperature and pressure is  $\sim 70$  nm, where the Knudsen number ( $K_n = \text{MFP}/l_{\text{char}}$ ,  $l_{\text{char}}$  is the characteristic dimension of the channel) is  $\sim 1$ , indicating the onset of free molecular flow.

The transport through 2D membranes, e.g. graphene membranes,<sup>34</sup> is governed by effusion due to the negligible thickness if the respective pore size is smaller than the MFP.

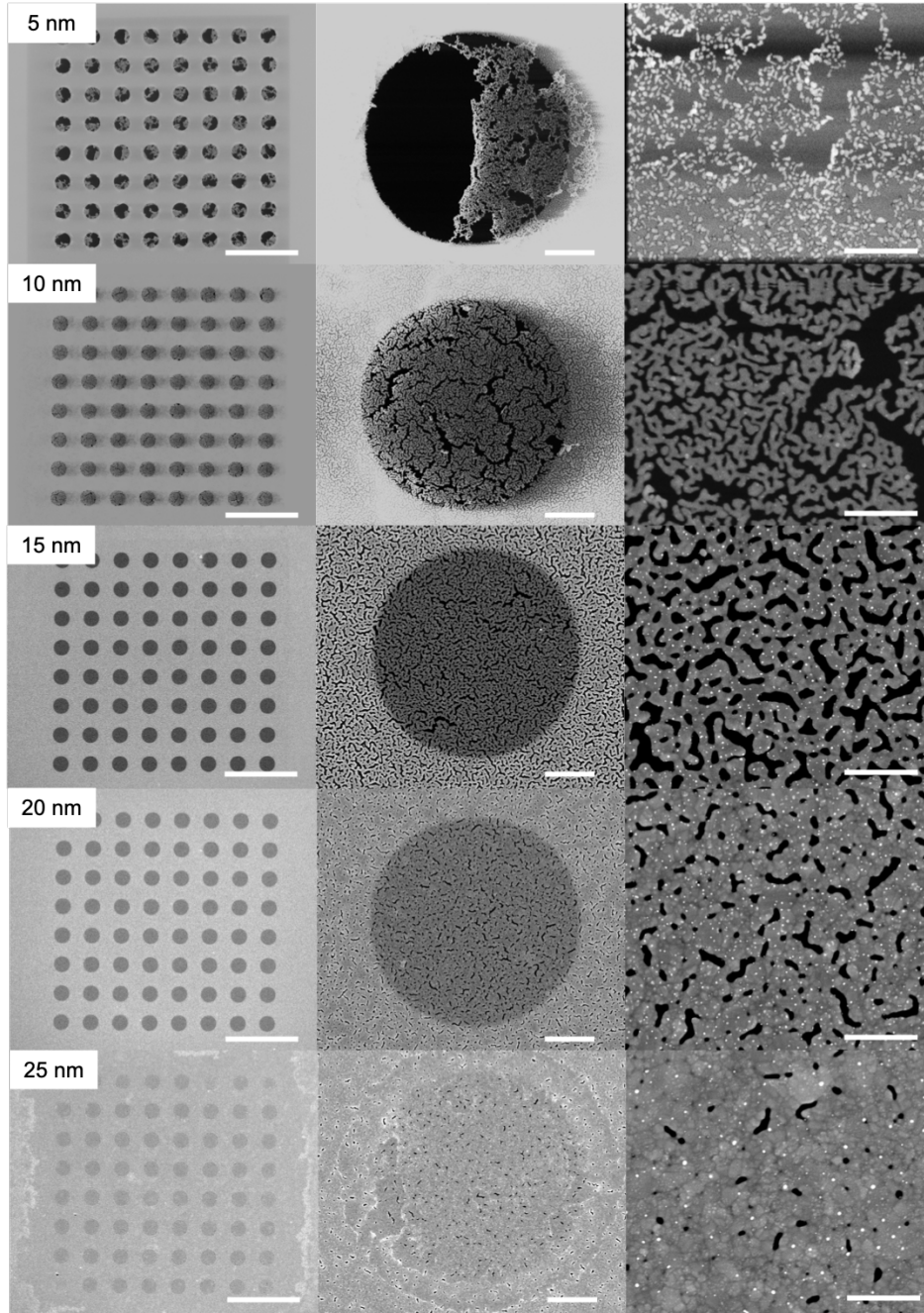


Figure 6: Full results of freestanding Au membranes from 5 nm (top) to 25 nm (bottom) in thickness, scale bars from left to right:  $20\ \mu\text{m}$ ,  $1\ \mu\text{m}$  and  $300\ \text{nm}$ . The 5 nm and 10 nm thick films cannot form a suspended membrane or exhibit cracks and fractures, so they are omitted in the subsequent investigation.

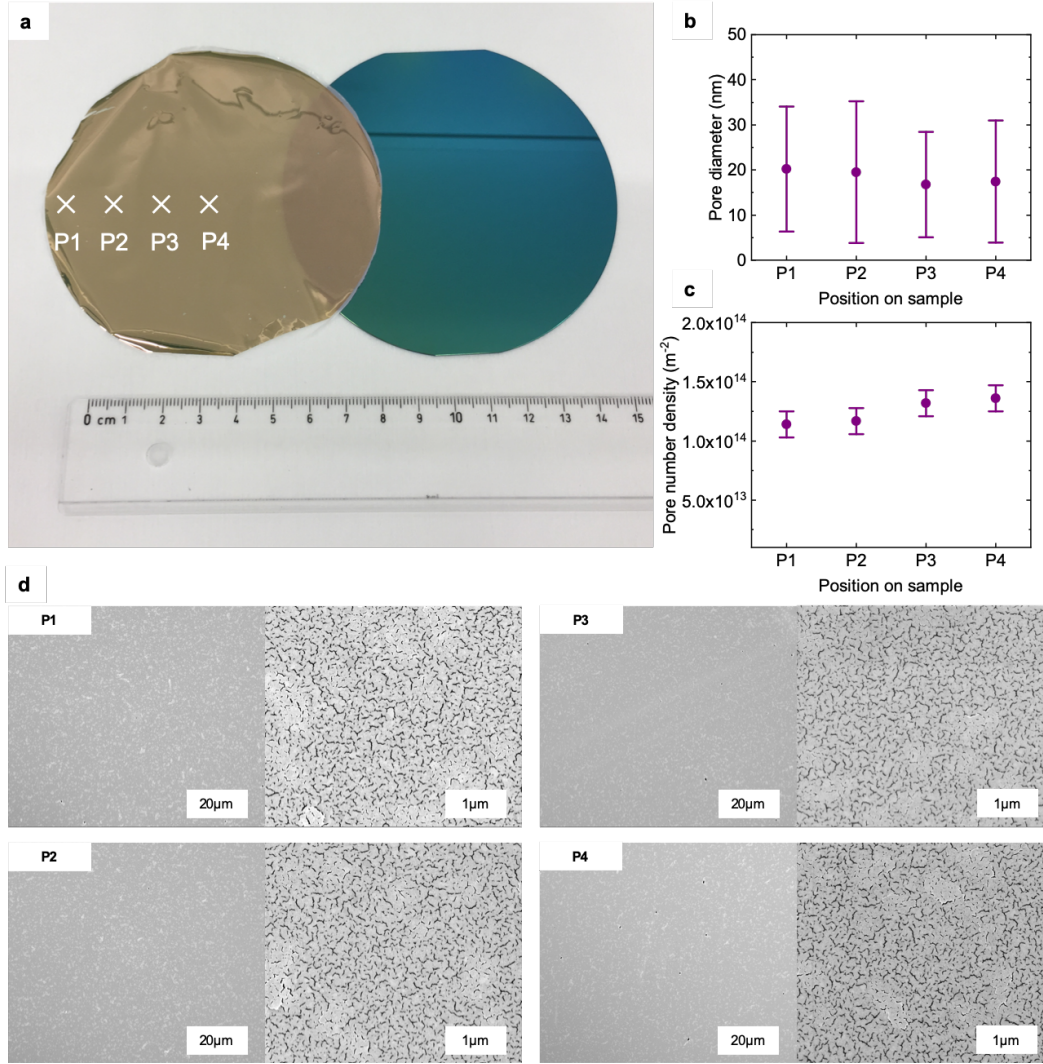


Figure 7: (a) 4-inch porous Au membranes on polycarbonate-track-etched (PCTE) with homogeneous (b) pore diameter and (c) pore number density extracted from four different location P1 to P4. In (d) the pores in the metal membrane are visible as black slits and dots, while the PCTE pores are visible as brighter regions in the background (see higher magnification SEM graphs). The metal was transferred to PCTE following the method developed in Ref.<sup>33</sup>

Effusion through a membrane with porosity  $\chi$  is given by

$$J = \frac{\chi}{\sqrt{2\pi MRT}}, \quad (3)$$

where  $M$  is the molar mass of  $N_2$  (0.028 kg/mol),  $R$  is the universal gas constant and  $T$  is the absolute temperature. It should be noted that in case of purely effusive transport the transport through an ensemble of pores is equivalent to the transport of a single pore with equivalent open area. In a system such as our gold membranes, having non-zero thickness  $t$ , however, the permeance based on effusion vastly overpredicts the mass transport, c.f. Fig. 2(e) of the main paper, in particular for lower porosities.

The proper way to describe the gas transport through our porous Au membrane is a combination of Knudsen Diffusion and Effusion.<sup>57</sup> However, the linear superposition as described in<sup>57</sup> was shown to be incorrect, leading to the introduction of transmission probabilities<sup>58</sup> instead, additionally taking into account the non-circular shape of the majority of the pores. As the pores in our PAuM have aspect ratios  $1 < a/b < 10$ , we calculate the permeance using the extreme cases that all pores are circular ( $a/b = 1$ , maximum permeance) and slit-like ( $a/b = 10$ , minimum permeance) to compare the corresponding range of values with our experimental data in Fig. 2(e). For membranes with low porosity (20 nm, 25 nm), the modelled and measured permeances agree well, while for 15 nm membranes, a higher permeance is measured than anticipated by the model. We attributed this behaviour to few larger holes in the membranes or the fact that  $t/D$  is small, so the thickness effect is negligible and the flow behavior is mostly effusive.

In this section, we model the gas transport through Au membranes and discuss the effect of the pores' shape on the permeation characteristics of the membrane. Fig. 8(a) schematically depicts a realistic pore shape distribution as it could be found in a membrane. Fig. 8(b) depicts the same pore area as in (a), however with circular pores and (c) depicts all pores with a high aspect ratio. Note that (b) and (c) correspond to the upper and lower

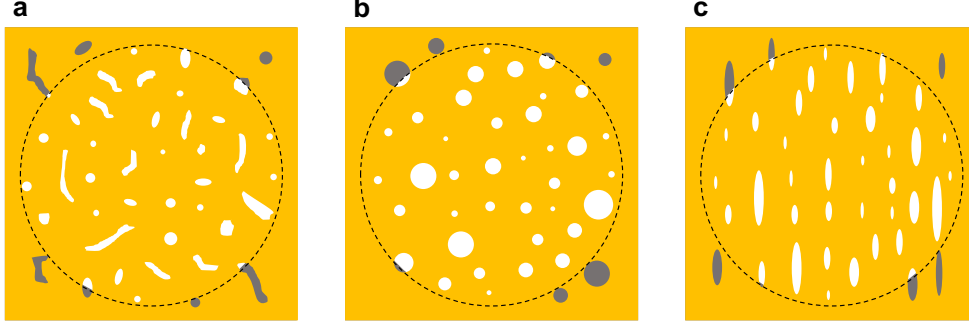


Figure 8: Schematic for modelling the gas transport through Au membranes with (a) realistic pore shapes, (b) circular pores having same areas as in (a) and (c) slit-like pores having same areas as in (a). The dashed black circle outlines the freestanding part of the membrane.

limit of permeation through a membrane with the corresponding pore size and thickness  $t$ .

(i) **Circular pores with depth  $t$ :** The extracted pore areas from ImageJ were converted into a radius of an equivalent pore. In Fig. 9, the histograms of the pore sizes ( $= 2\bar{r}$ ) for the membranes 15 nm - 25 nm are shown, where the black dashed line marks a corresponding log-normal distribution.

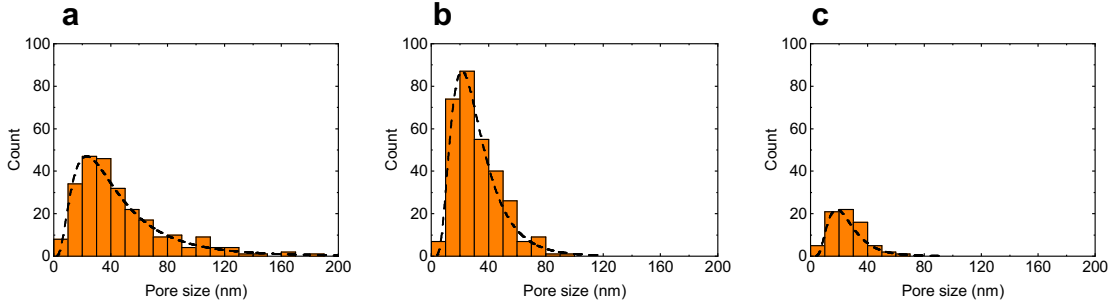


Figure 9: Pore size ( $= 2\bar{r}$ ) histograms of (a) 15nm, (b) 20nm and (c) 25nm Au membranes. The black dashed line marks a corresponding log-normal distribution.

The log-normal distribution is characterized by the distribution function  $P(m,s)$ , where  $m$  and  $s$  are the mean and standard deviation of the natural logarithm of the pore radius, respectively. The corresponding pore radius and standard deviation are denoted  $\bar{r}$  and  $\sigma_{\bar{r}}$ , respectively, and are shown in Table 3.

$t/\bar{r}$  denotes the average ratio of thickness to pore size, with  $t/\bar{r}_{upper}$  and  $t/\bar{r}_{lower}$  being the upper and lower limit of the ratio based on the average pore size. The corresponding

thickness-dependent transmission probabilities  $W_t$  are tabulated,<sup>58</sup> where  $Q = Q_e * W_t$ ,  $Q$  is the real permeance and  $Q_e$  is the purely effusive permeance. Based on the transmission probabilities and assuming circular pores with depth  $t$ , one can expect permeances to be reduced up to 62% of the original value (shown as round dots in Fig. 1e). The remaining discrepancy can be attributed the effect of pore shape.

(ii) **Slit-like pores with depth  $t$ :** A factor that has been neglected was the pore shape, assuming circular pores previously to allow a more simple modelling. A significant portion of pores in the membrane is, however, non-circular/slit-like. The problem has been studied for long tubes, where at equal area, the gas transport through non-circular pores is always lower compared to a circular pore.<sup>59</sup> For example, the permeance of a slit  $Q_e$  with an aspect ratio of  $a/b = 1/10$  is reduced by a shape dependent factor  $W_s$  of 0.26 compared to the permeance  $Q_c$  circular pore of the same area (*i.e*  $Q_e = W_s * Q_c$ ). It is intuitive to assume that the flow rate through a short elliptical aperture is therefore reduced compared to a circular aperture, however, the exact factor has yet to be established. The values given in Fig. 2(e) of the main paper therefore show the data assuming round pores.

## Freestanding graphene as Raman reference

Natural graphite was mechanically exfoliated onto an oxidized silicon wafer. A monolayer was identified optically, see,<sup>60</sup> and then transferred to a patterned silicon nitride (SiN) membrane shown in Fig. 10 following the procedure outlined in Ref.<sup>54</sup> Reference Raman spectra were obtained by focusing the laser centrally on the monolayer graphene suspended of the

Table 3: Average pore size, standard deviation of Au membranes based on log-normal distribution, thickness-to-pore-size-ratio and the corresponding transmission probabilities  $W$ .

Membrane	$m$ (-)	$s$ (-)	$\bar{r}$ (nm)	$\sigma_{\bar{r}}$ (nm)	$t/\bar{r}$	$t/\bar{r}_{upper}$	$t/\bar{r}_{lower}$	W
15 nm	2.92	0.699	23.9	19	0.63	0.35	3.06	0.38 - 0.86
20 nm	2.6	0.52	16	8.91	1.25	0.8	2.82	0.43 - 0.71
25 nm	2.44	0.49	13.06	6.82	1.83	1.22	3.7	0.38 - 0.63



circular holes in the SiN membrane. The SERS Raman spectra in Fig. 3 of the main paper were normalized to the  $2D$ -intensity (integrated area) of suspended graphene. To obtain the enhancement factors given in Table 1 of the main paper, we normalized the SERS intensities of the  $G$ - and  $2D$ -modes individually to the corresponding intensities of the suspended graphene Raman reference for each excitation wavelength.

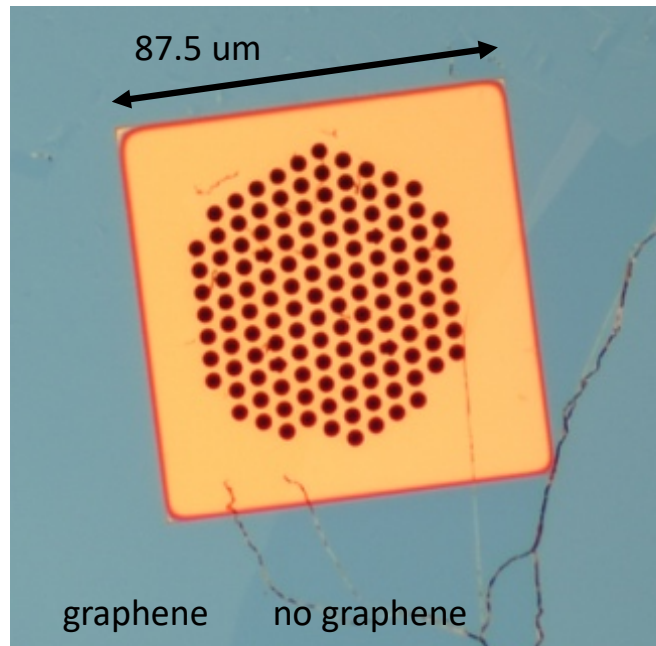


Figure 10: Mechanically exfoliated graphene suspended over a patterned SiN membrane were used as Raman reference. The contrast outside the patterned area indicated that most of the holes are covered by graphene.

# SERS of two additional graphene covered, suspended Au-membranes

In this section we present the SERS enhancement of two additional graphene-covered, suspended Au-membranes shown Figs. 11 and . 12, respectively. The experimentally observed SERS enhancement is summarized in Table 4, while the comparison to numerical simulations for both membranes is shown in Fig. 13.

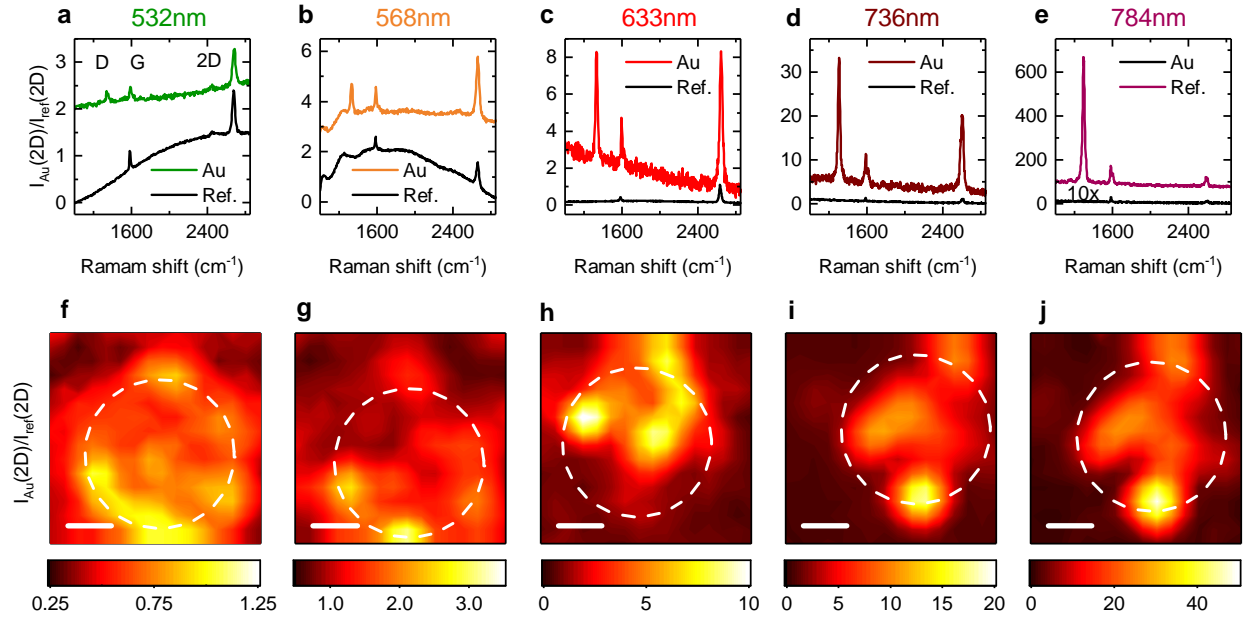


Figure 11: 2D-mode SERS enhancement map of graphene placed on freestanding Au membrane AuM-R1 for five excitation wavelength. The intensity is normalized to the 2D-mode of freestanding graphene. (a-e) Raman spectra(red) extracted from the Raman maps (f-j) at the location of the highest 2D enhancement together with reference spectra (black) of freestanding graphene. The scale bar in (f-j) is 500 nm.

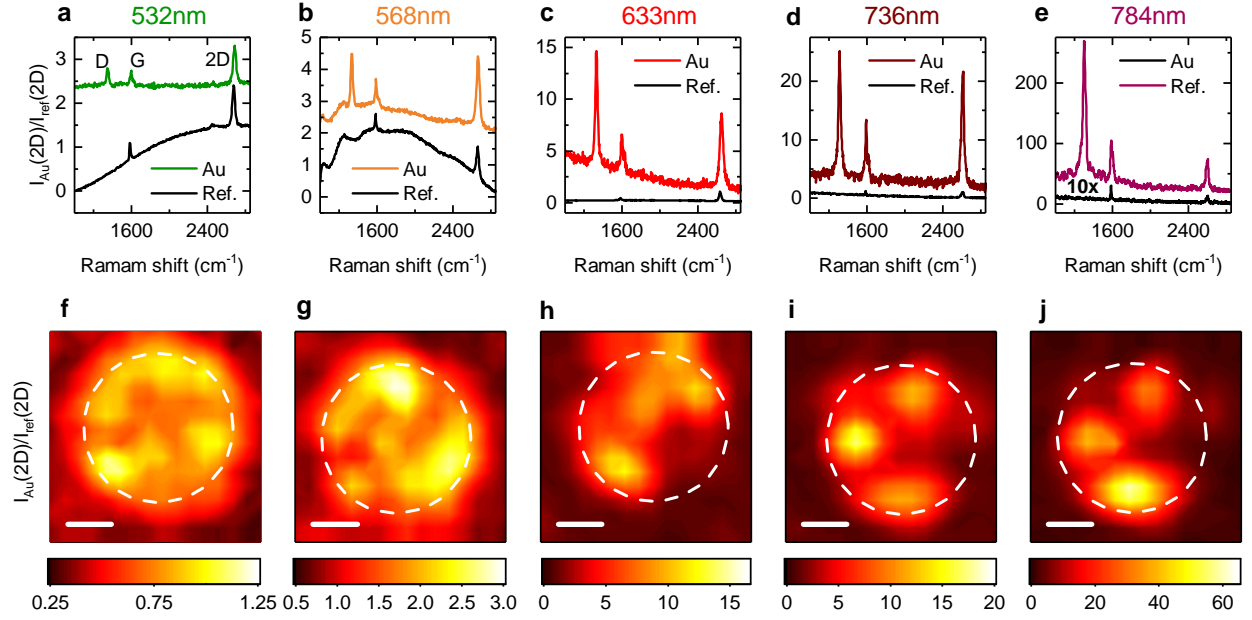


Figure 12: 2D-mode SERS enhancement map of graphene placed on freestanding Au membrane AuM-R2 for five excitation wavelength. The intensity is normalized to the 2D-mode of freestanding graphene. (a-e) Raman spectra (red) extracted from the Raman maps (f-j) at the location of the highest 2D enhancement together with reference spectra (black) of freestanding graphene. The scale bar in (f-j) is 500 nm.

Table 4: Summary of SERS enhancement factors of the G- and 2D mode at locations of highest intensity for the freestanding PAuM in the main paper, and the two additional PAuM (PAuM-R1 see Fig. 11 , PAuM-R2 see Fig. 12) for different excitation wavelengths.

$\lambda(\text{nm})$	532	568	633	736	784	
$\text{EF}_G$	0.9	3.0	13.3	169	202	main paper
$\text{EF}_{2D}$	1.0	4.3	10.5	42.7	60.0	main paper
$\text{EF}_G$	1.3	2.2	20.3	30.5	62.8	AuM-R1
$\text{EF}_{2D}$	1.1	2.90	12.0	24.0	54.8	AuM-R1
$\text{EF}_G$	1.0	2.2	8.8	18.7	56.6	AuM-R2
$\text{EF}_{2D}$	1.0	3	9.7	22.3	46.1	AuM-R3

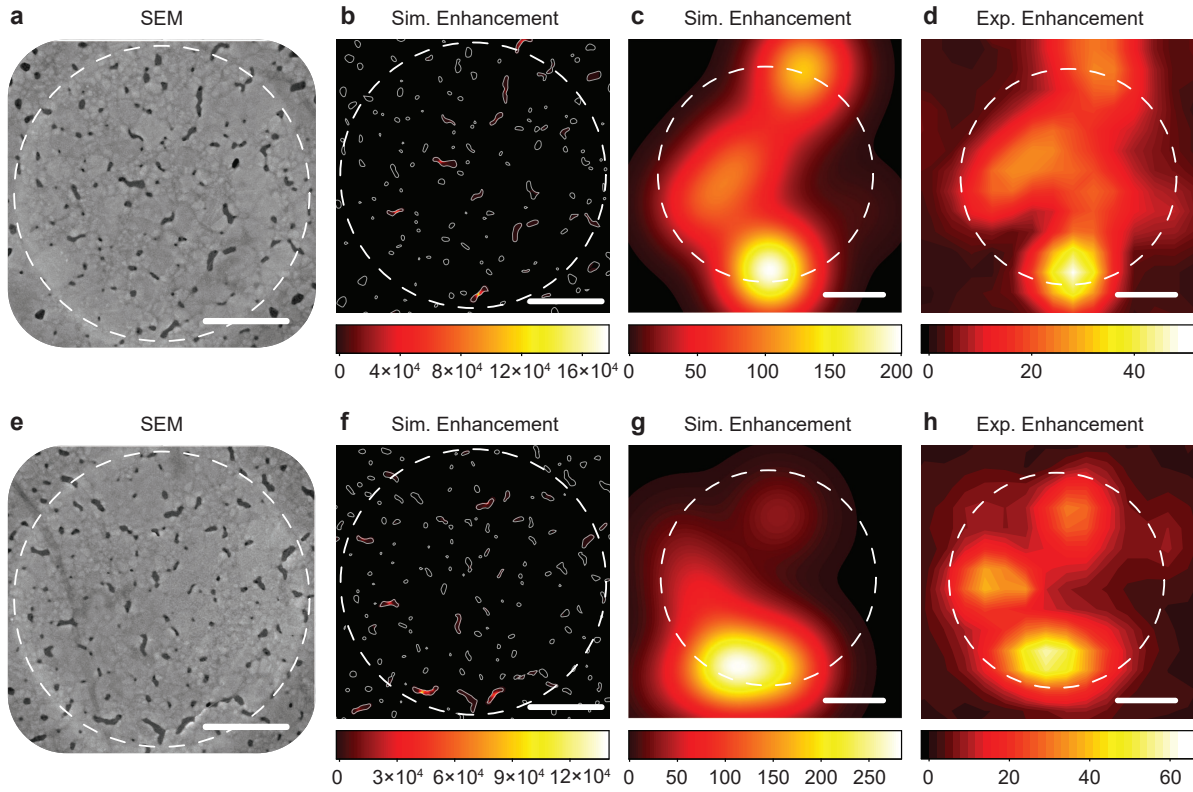


Figure 13: Numerical analysis of two additional porous Au membranes (PAuM-R1/R2, see Fig. 12). (a,e) SEM images of a freestanding Au membranes (25 nm nominal thickness), covered by monolayer graphene. (b,f) Simulated local enhancement  $\text{EF}_{\text{loc}}$  (cf. main text) of the 2D Raman mode intensity for an excitation wavelength  $\lambda_{\text{exc}}$  of 784 nm, overlayed with the outlines extracted from (a,e). (c,g) As (b,f), convoluted with a Gaussian function, the full width at half maximum (FWHM) of which is given by  $\lambda_{\text{exc}}/(2\text{NA})$ , where  $\text{NA} = 0.8$  is the numerical aperture of the objective. (d,h) Experimental map of the enhancement of the integrated 2D intensity at  $\lambda_{\text{exc}} = 784\text{ nm}$ , reproducing the data shown in Fig. 11(j) and Fig. 12(j), respectively. The dashed outlines mark the position of the suspended membrane. Scale bar is 500 nm.

# Numerical analysis of regular slot antennas in a thin Au film.

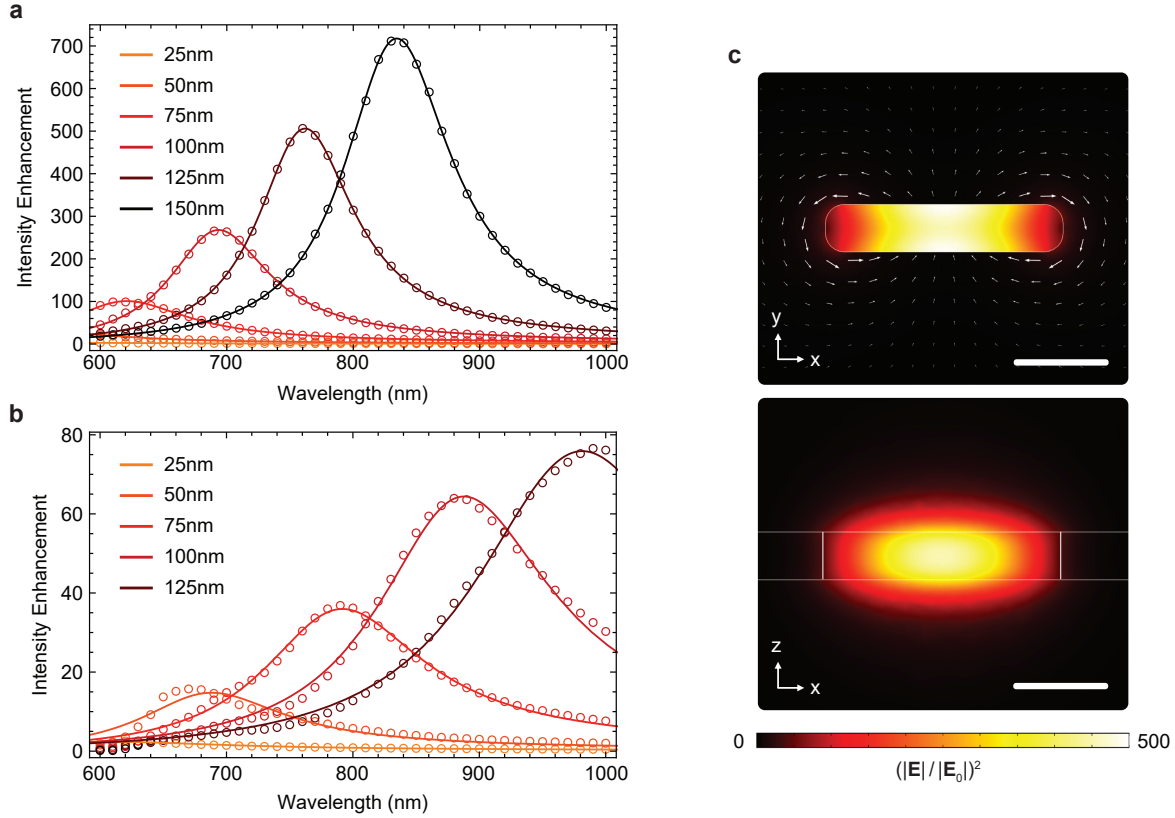


Figure 14: Numerical analysis of regular slot antennas in a thin Au film. (a) Simulated intensity enhancement  $|\mathbf{E}|^2/|\mathbf{E}_0|^2$  in the geometrical center of rectangular slots of constant width  $w = 25 \text{ nm}$  and height  $h = 25 \text{ nm}$ , a corner radius of  $10 \text{ nm}$  and varying length ranging from  $25 \text{ nm}$  to  $150 \text{ nm}$  in steps of  $25 \text{ nm}$ . The slots are suspended (surrounded by air) and illuminated with plane waves, polarized parallel to their short axis. (b) As (a) but for supported slot antennas ( $\text{Si}_3\text{N}_4$  substrate with a refractive index of  $n = 2$ ). Simulations are carried out as a function of wavelength (circles), fitted by Lorentzian functions (lines). (c) Cross sectional intensity enhancement distribution of a  $125 \times 25 \times 25 \text{ nm}^3$  suspended slot antenna within a  $x$ - $y$ -plane (top) and a  $x$ - $z$ -plane (bottom) through the center of the slot antenna. White arrows indicate magnitude and direction of the current density. Scale bar is  $50 \text{ nm}$ .

## SERS stability under high illumination powers

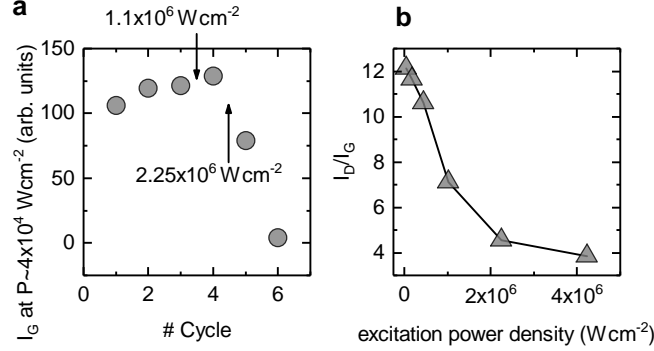


Figure 15: (a) G-mode intensity at nanopore SERS hotspot measured with low excitation power densities  $P$  after every increase in  $P$ . For  $P_{\min} > 1.1 \times 10^6 \text{ Wcm}^{-2}$ , the decrease of the the G-mode intensity indicates the onset of irreversiabile damage to the graphene at the SERS hotspot. (b)  $I_D/I_G$  ratio as a function of  $P$ , demonstrating the restoration of defects at the SERS hotspot with increasing temperature.

In Fig. 15(a) we present the G-mode intensity measured at  $P_{\min} \sim 4 \times 10^4 \text{ Wcm}^{-2}$  after every increase in excitation power density  $P$ , which serves as a control measurement to ensure that the graphene/nanopore system forming the SERS hotspot is stable with every increase in illumination power. The G-mode intensity remains approximately constant up to  $P = 1.1 \times 10^6 \text{ Wcm}^{-2}$ , and drops for  $P > 2.25 \times 10^6 \text{ Wcm}^{-2}$ , which indicates the failure of the graphene/nanopore hotspot, see main paper.

We cannot use the graphene D-mode, which indicates the presence of defects, to monitor the onset of damage with increasing  $P$  because the nonzero intrinsic defect density in the CVD graphene used to probe the nanopore hotspot. In fact, the  $I_D/I_G$  ratio which typically serves as an indicator for the defect density, counterintuitively decreases with increasing excitation power density as shown in Fig. 15. We explain this behaviour by the increase in temperature at the hotspot with increasing excitation power, c.f. main paper, as certain types of defects in graphene have low restoration energies such that defects in the graphene membrane can effectively be repaired at moderate temperatures.<sup>61</sup>

In Table 5, we list a representative set of SERS structure including the powerthreshold to

Table 5: Comparison of maximum power densities used for a variety of SERS structures and the porous Au membranes introduced in this work.

Structure	fabrication	probe	$\lambda$ [nm]	power [W/cm <sup>-2</sup> ]	Ref.
Au dimers with sub-nm gaps	e-beam	molecules	700 - 900	$2.2 \times 10^3$	15
Silver nanodiscs	e-beam	molecules	633	$5.5 \times 10^4$	6
Au Nanotriangles	self-assembly	molecules	633 & 785	$1.7 - 6.9 \times 10^3$	7
"Sea urchin" Au mesoparticles	self-assembly	molecules	633 & 785	$1.4 - 6.4 \times 10^3$	8
Au nanodot arrays	mask lithography	molecules	633	1.2	9
Au dimers	e-beam	graphene	633	$5 \times 10^4$	16
Au dimers	e-beam	graphene	633	$5 \times 10^4$	14
PAuM	evaporation	graphene	532-785	$1.1 \times 10^6$	this work

avoid damage. The PAuM introduced in this work exceed all other structures by 2-3 orders of magnitude.

## Large-scale SERS mapping of 20 nm thick porous Au membrane

Figure 16 shows a large scale 2D-mode SERS map of 15 freestanding PAuM segments covered with graphene for 633 nm excitation. Taking into account the locations of maximum enhancement of each circular segment, we obtain an average 2D-mode enhancement of  $19 \pm 6$ , which is a factor of 1.73 larger than for the three freestanding segments of the 25 nm thick PAuM ( $11 \pm 1$ , see main paper). The increase in SERS enhancement is in good agreement with the corresponding 1.9-fold increase in pore density from  $4.4 \times 10^{13} \text{ m}^{-2}$  for the 25 nm membrane to  $8.5 \times 10^{13} \text{ m}^{-2}$  for the 20 nm, see Figure 2 of the main paper. We conclude that the total SERS enhancement increases approximately linearly with the pore density number of the porous Au membranes for thicknesses of 15-25 nm as investigated here.

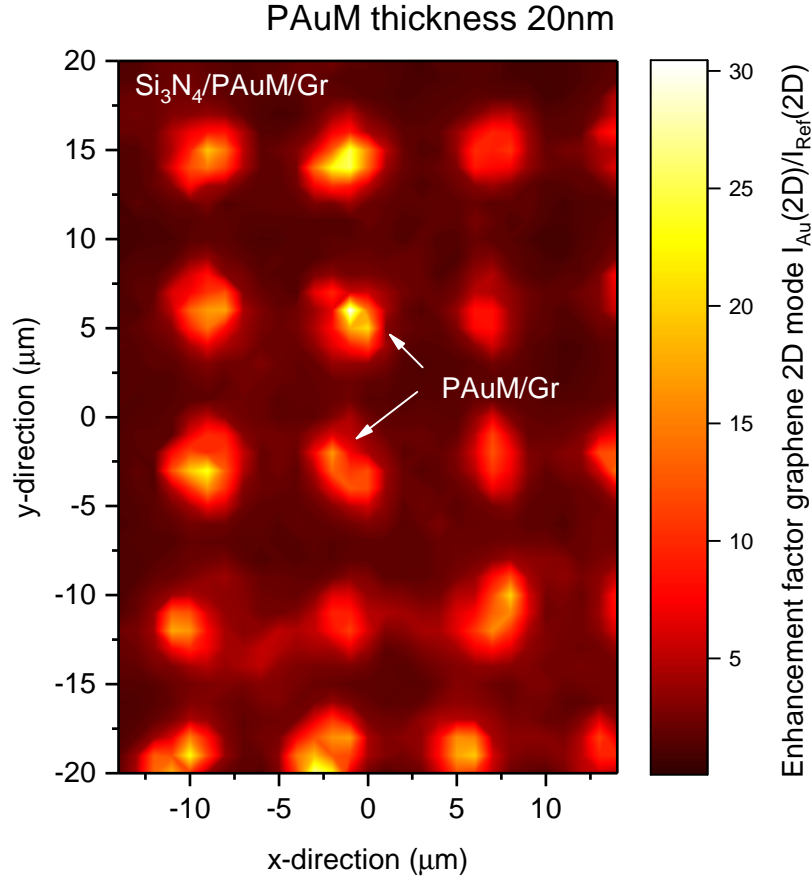


Figure 16: Large-scale SERS map of the 2D-mode of graphene placed on top of a 20 nm PAuM for an excitation wavelength 633 nm. As in the main paper, the enhancement is given using freely suspended graphene as reference. SERS enhancement occurs predominantly at the circular, freestanding PAuM regions, and is barely present in the areas supported by the Si<sub>3</sub>N<sub>4</sub> frame.